Influence of Non-Expansive Clay on the Hydration and Microstructure of Recycled Cement

José Alexandre Bogas[1], Ricardo Cruz[1], Mafalda Guedes[2,3], João Abrantes[4]

[1] CERIS, Instituto Superior Técnico, Universidade de Lisboa, Av. Rovisco Pais, 1, 1049-001 Lisboa, Portugal
[2] DEM, Instituto Superior de Engenharia de Lisboa, Instituto Politécnico de Lisboa, Rua Conselheiro Emídio Navarro 1, 1959-007 Lisboa, Portugal.
[3] CeFEMA-LaPMET, Instituto Superior Técnico, Universidade de Lisboa, Av. Rovisco Pais, 1049-001 Lisboa, Portugal.
[4] proMetheus, Instituto Politécnico de Viana do Castelo, 4900-347, Viana Do Castelo, Portugal

Abstract:

This study investigates the effect of a non-expanding, kaolinite-rich clay on the hydration behaviour, microstructural development, and mechanical strength of recycled cement (RC), with ordinary Portland cement (PC) used for comparison. The aim is to better understand and support the use of RC as a more environmentally sustainable alternative for earth stabilisation. Clay–cement pastes were produced by replacing 25 vol.% of cement with kaolinite, using high water-to-cement ratios representative of earth-based construction materials. Mixes containing inert quartz served as references. Hydration kinetics, phase assemblage, pore structure, and strength development were assessed by thermogravimetric analysis, X-ray diffraction, nuclear magnetic resonance spectroscopy, mercury intrusion porosimetry, nitrogen adsorption, scanning electron microscopy, and mechanical testing.

Results showed that the non-expanding clay did not delay early hydration of either PC or RC. In PC pastes, kaolinite slightly accelerated hydration, leading to a higher degree of hydration and slightly more polymerized calcium silicate hydrate. In RC pastes, the inherently high reactivity and large specific surface area of RC dominated the hydration behaviour, reducing the relative influence of clay addition. No significant pozzolanic reactivity of the clay was detected, with cement–clay interactions limited to minor surface effects. Microstructural analysis indicated that RC pastes developed a finer pore structure than PC pastes at the same w/c, while clay affected the microstructure primarily through physical mechanisms. Overall, the findings demonstrate that non-expansive kaolinitic clay does not adversely affect RC hydration or microstructure, supporting the use of RC as a sustainable stabiliser in earth construction.

Keywords: recycled cement; clay; kaolinite; hydration; microstructure; mechanical strength

1. Introduction

Clay minerals are naturally present in soils and are widely recognized as problematic in construction due to their strong affinity for water and moisture-sensitive behaviour [1,2]. As a result, chemical stabilisation is essential in earth construction to enhance the material's inherent low strength, cohesion, and water resistance, ensuring compliance with modern performance requirements [3]. Among stabilisers, ordinary Portland cement (PC) remains the most widely used due to its effectiveness in reducing the plasticity, swelling, and compressibility of clayey earth, while significantly enhancing its strength and durability [1,4,5]. Cement stabilisation primarily involves the mechanisms of ion exchange, flocculation–agglomeration, and cementation [2]. Clay minerals are hydrated aluminosilicates smaller than 2 µm, characterised by residual negative surface charges resulting from the partial substitution of aluminium by iron and/or magnesium within their structure [1,6]. Depending on their structural configuration, clays vary from 1:1 type, such as kaolinite, to 2:1 type, such as smectite, the latter exhibiting higher cation exchange capacity (CEC), water absorption and swelling potential [7–9]. However, this behaviour depends on the type of interlayer cations. For example, in 2:1 illite, tightly bound K^+ ions restrict swelling and reduce d-spacing, resulting in behaviour similar to non-swelling 1:1 kaolinite [6]. When calcium-based stabilisers are mixed with clay, monovalent interlayer cations are replaced by Ca^{2+}, reducing interlayer spacing and increasing electrolyte concentration. This induces flocculation and agglomeration, transforming the clay's plate-like structure from a flat-parallel to a random edge-to-face orientation. This rearrangement decreases plasticity and contributes to early strength gain through weak interparticle bonding [2,10]. Over time, cement hydration forms calcium silicate and aluminate hydrates that bind clay particles, increase cohesion, and reduce porosity, thereby producing a microstructure that is less susceptible to moisture-induced dimensional changes [1,10–12].

Although the overall cementation mechanism is well established, the influence of clay minerals on cement hydration, microstructural development, and secondary reactions remains insufficiently understood. It is suggested that clay minerals may interfere with hydration by competing for water or by adsorbing Ca^{2+} ions, thereby affecting setting and reaction kinetics [1,6,13–15]. Experimental evidence appears contradictory. In some cases,

clay minerals are reported to delay setting and reduce strength due to cement grain encapsulation and high water demand [16–18], whereas other studies indicate accelerated hydration attributed to nucleation effects and ion release from clay surfaces [7,19–21]. The response appears highly dependent on clay type, exchangeable cations, replacement level, and mixture design, leading to inconsistent conclusions. For example, Krøyer et al. [7], using ^{29}Si NMR, reported that kaolinite accelerated alite hydration and increased Q^2 species formation. However, Lindgreen et al. [20] observed hydration acceleration with montmorillonite, but not with kaolinite, in cement systems with 10% clay replacement. In contrast, Muñoz et al. [21], based on XRD and SEM analyses, found accelerated hydration with kaolinite and Ca-montmorillonite, whereas Na-montmorillonite showed a retarding effect.

Secondary pozzolanic reactions in cement-clay systems have also been proposed [10,12,19,22]. Following clinker dissolution and the resulting increase in pH, the highly alkaline environment may dissolve the amorphous silica and alumina in clay minerals and, subsequently, react with calcium hydroxide to form additional C–S–H and C–A–H phases [19,23]. Evidence of such reactions varies. While some studies report clay consumption and formation of secondary hydrates [1,24], others found no clear evidence of significant pozzolanic activity, consistent with the low reactivity of raw crystalline clays [7,25,26]. Consequently, the relevance of secondary reactions in cement–clay systems remain debatable.

Clay minerals are generally considered detrimental to cement-based materials, and standards impose strict limits on allowable clay contents [6,13]. This is primarily due to their high-water absorption, weak mechanical properties, and poor bonding with aggregates [15,19,25,27]. Nevertheless, reported effects on mechanical performance varies widely, with both strength reductions and improvements documented depending on factors, such as the clay type, dosage, dispersion conditions, and water-to-cement (w/c) ratio [24,25,28–33]. In cement-stabilized earth materials, especially at high water contents, w/c ratio is a dominant factor controlling strength development [4,25]. Because clays increase water demand, comparisons using different w/c ratios can be misleading. Therefore, clay effects should be assessed using cement–clay mixes with similar w/c ratios.

Beyond technical challenges, cement stabilisation raises sustainability concerns due to the high environmental impact of PC [34]. This has driven interest in alternative low-clinker

binders and supplementary cementitious materials [35–37]. Among these, thermoactivated recycled cement (RC), produced by heating at 600–800 ºC the cement paste fraction recovered from concrete waste, has emerged as a promising eco-efficient stabiliser [38,39]. Previous studies have demonstrated the high rehydration capacity of RC, which shows comparable mechanical strength to CEM I 32.5 [39–42]. RC hydration involves similar reaction stages to PC, but the primary anhydrous compound is α'_H-C_2S, which reacts faster than belite, typically within 1-3 days [46]. Moreover, RC hydration results in a finer, dual-porosity microstructure, composed of both intra- and inter-particle porosity, linked to the porous nature of RC and the surrounding matrix, respectively [45]. A drawback of RC is its higher water demand due to its porous structure [43,44]. Nevertheless, replacing up to 40% of OPC with RC has been shown to have little effect on the mechanical and durability performance of concrete [41,42]. A major challenge in RC production is the recovery of cement paste from concrete waste. To address this, the authors previously developed a low-energy separation process achieving cement paste purities above 75 wt.% [47]. This enables the production of RC with carbon emissions more than 75% lower than those of PC [34,48–50]. Recycled cement has demonstrated strong potential as an earth stabiliser, significantly improving the strength and water resistance of compressed earth blocks (CEB) [51–53], while maintaining favourable thermal and hygroscopic properties [54,55]. However, the interactions between RC and clay minerals, and their influence on hydration and strength development remain unexplored.

To fill this gap, this study examines clay–RC interactions, focusing on hydration kinetics and microstructural development. A kaolinite-rich clay was blended with either RC or PC in high w/c pastes. Phase development and pore structure were monitored over time using X-ray diffraction (XRD), thermogravimetry (TG), nuclear magnetic resonance spectroscopy (NMR), scanning electron microscopy (SEM), mercury intrusion porosimetry (MIP), and nitrogen adsorption (N_2A), alongside mechanical strength development. A kaolinite-rich clay was selected for its abundance, low reactivity, and non-swelling behaviour, similar to illite. These characteristics make it more suitable for cement stabilization in earth construction than expansive clay minerals [56]. Additionally, kaolinite is less prone to aggregation, helping to better understand the clay−cement interaction [19,57]. Inert quartz sand was used in reference mixes in place of kaolinite to isolate physical filler effects. Plain PC pastes were also characterised for comparison. The objectives of this study are twofold:

to investigate clay–RC interactions and to improve understanding of stabilization kinetics in cement systems.

2. Experimental campaign

2.1 Raw materials

A pre-processed kaolinite-rich clay was selected. Owing to its high purity and non-swelling behaviour, the material is considered representative and well suited for investigating clay-cement interaction mechanisms in earth-based construction materials. The chemical composition and main physical properties of this clay are summarized in Table 1. X-ray diffraction (XRD) analysis identified kaolinite, illite/muscovite, and quartz as the dominant mineral phases (Figure 1). Based on chemical composition and approximate phase stoichiometry, their average contents were estimated at 63%, 23%, and 14%, respectively. For simplicity, the clay is hereafter referred to as kaolinite. Particle size distribution was measured by wet laser granulometry using a Malvern Mastersizer 3000, after ultrasonication (Figure 2). The kaolinite was supplied as a powder composed of fine aggregates of plate-like particles (Figure 3).

For comparison, inert quartz fine sand was used in the reference mixtures as a replacement for the clay fraction. This approach allowed the isolation of the effects associated with clay-cement interactions. However, the quartz sand exhibited a slightly coarser particle size distribution (Figure 2) and a lower specific surface area (SSA) than the kaolinite (Table 1).

Table 1 – Chemical analysis and physical properties of quartz fine sand, kaolinite-rich clay, Portland cement (PC), recycled cement (RC).

Parameter		Standard	Quartz	Kaolinite	PC	RC
Density (kg/m^3)		[a]	2690	2740	3030	3007
BET surface area (m^2/g)		−	1.08	13.8	1.97	9.8
d_m (mm)		−	17.7	11.5	21.3	25.5
Free CaO (%)		EN 451-1 [58]	0.00	0.00	2.73	13.94
$SiO_2 + Al_2O_3 + Fe_2O_3$ (%)		EN 196-2 [59]	99.0 + 0.1 + 0.1	53.2 + 33.3 + 1.7	19.5 + 5.0 + 2.9	19.1 + 5.1 + 3.0
CaO + MgO (%)		EN 196-2 [59]	0.0 + 0.0	0.0 + 0.3	63.0 + 1.6	60.8 + 1.8
Water requirement		EN 196−3 [60]	Not applicable		0.30	0.74
Setting time (min)	Initial	EN 196−3 [60]			158	375
	Final				236	415

[a] by helium pycnometry

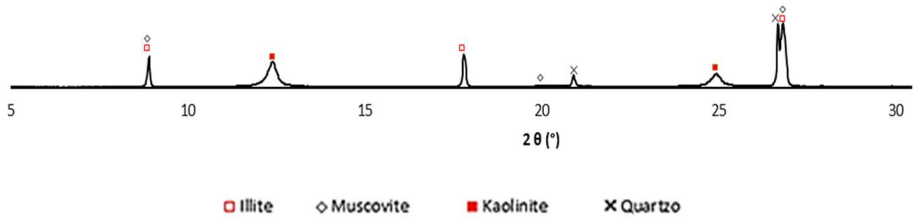

Figure 1 – X-ray diffraction analysis of kaolin clay.

Recycled cement (RC) and a reference Portland cement (CEM I 42.5R, denoted PC) were used as stabilisers. The RC was produced from laboratory-prepared cement pastes made with PC at a w/c ratio of 0.55. Artificial cement pastes were used in place of concrete waste to minimise variability associated with aggregate contamination, thereby allowing clearer analysis of clay–cement interactions. Previous studies have shown that RC retrieved from separated concrete waste exhibits binding properties comparable to those of RC obtained from pure cement paste [41,51]. In addition, Carriço et al. [40] reported that RC properties are only marginally influenced by the w/c ratio of the source cement waste. The cement pastes were cast into 150 mm cubes and subjected to 7 days of wet curing, followed by more than 4 months of storage under ambient conditions (60–80% relative humidity, RH). The hardened pastes were then crushed, ground, and milled to a particle size below 150 μm, before undergoing thermal activation in a rotary kiln at a heating rate of 10 °C/min to 650 ºC, with holding periods of 1 h at 150 ºC and 3 h at 650 ºC. The main physical properties of RC and PC are summarised in Table 1. RC exhibited a SSA roughly five times higher than that of PC, due to its porous structure and irregular particle morphology [43,45]. This characteristic significantly increases the water demand of RC, which is more than twice that of PC (Table 1).

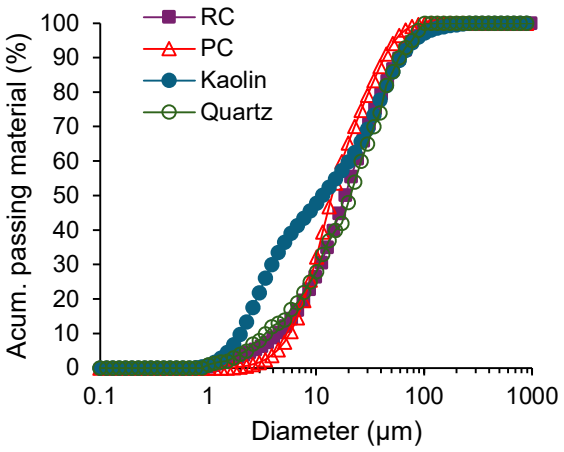

Figure 2 – Particle size distribution of PC, RC, Kaolinite and Quartz.

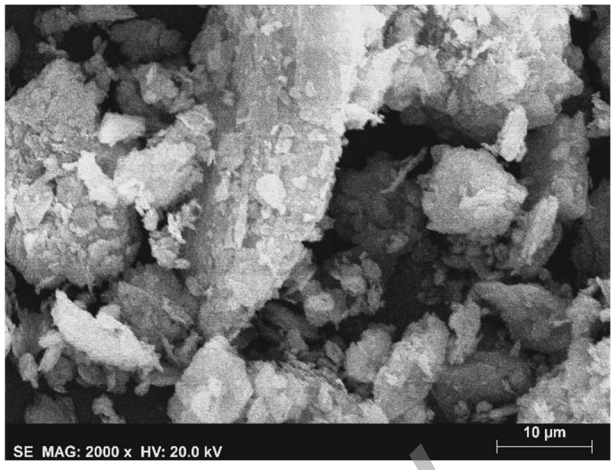

Figure 3 – SEM of kaolinite-rich clay.

The pozzolanic activity of the kaolinitic clay was assessed using the Frattini test for pozzolanic cements, according to EN 196−5 [61]. The concentrations of Ca^{2+} and OH^- released into an aqueous solution in contact with a blend containing 80 wt.% PC and 20 wt.% kaolin were measured after 8 and 15 days of storage at 40 ºC. As shown in Figure 4, the results for the PC–clay blend plot above the calcium ion saturation curve, indicating that the kaolinitic clay does not exhibit pozzolanic activity under the tested conditions. The same procedure was applied to quartz sand and a reference pozzolanic fly ash, confirming their inert and pozzolanic behaviour, respectively.

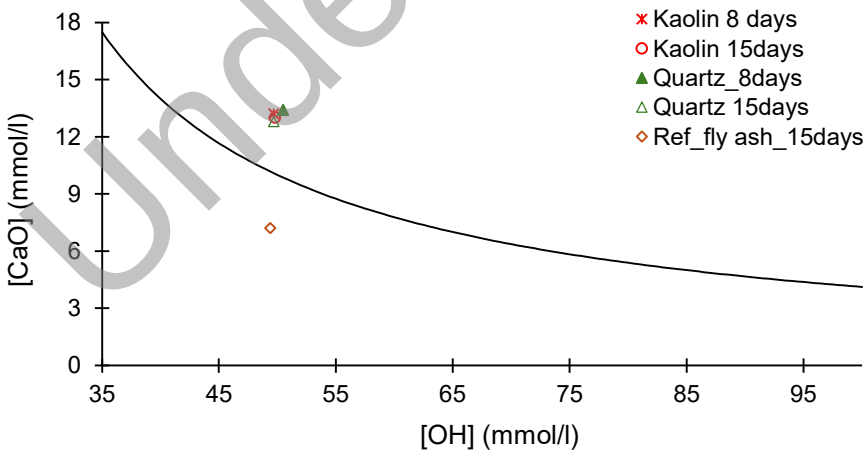

Figure 4 – Pozzolanicity of pozzolanic cements according to EN 196-5 [61] at 8 and 15 days.

2.2 Specimen production

The paste compositions are summarised in Table 2. Clay–cement pastes were prepared by replacing 25 vol.% of PC or RC with kaolinite (CK and RCK), targeting a flow spread of

160–190 mm, according to EN 1015−3 [62]. As noted, reference pastes in which the clay was replaced by an equivalent volume of inert quartz (CQ and RCQ) were also prepared for comparison. At high cement contents (above approximately 60 vol.%), clay particles are embedded within a continuous cement paste matrix, and the mechanical performance is predominantly governed by the w/c ratio [4]. In the present study, for each stabiliser type, the total volume of solids (cement plus additions) and the w/c were kept constant across mixtures. However, owing to its higher water demand, RC−based pastes were produced with a w/c of 1.0, whereas PC-based pastes were prepared with a w/c of 0.52. To enable a more direct comparison of the influence of clay on the two types of stabilisers, an additional PC–kaolinite mixture (CK1) was prepared with the same w/c ratio as the RC-kaolinite paste. Furthermore, reference mixtures containing only PC or only RC, but with the same w/c as the corresponding clay–cement pastes, were produced. Using high w/c and high cement-to-clay ratios in this study provides favourable conditions for promoting and assessing clay–cement interactions.

Table 2 – Compositions of the produced pastes.

Mix	**Addition (ad)**			**w/c**	**w/(c+ad)**	**M_{binder}**	**M_{cem}**	**M_{ad}**	**M_w**
	Type	(vol.%)	(wt.%)			(kg/m^3)	(kg/m^3)	(kg/m^3)	(kg/m^3)
C	-	-	-	0.52	0.52	1120	1120	0	583
RC	-	-	-	1	1	713	713	0	713
CQ	Q	25	22.7	0.52	0.40	1284	993	292	516
RCQ	Q	25	23.0	1	0.77	854	658	196	658
CK	K	25	23.0	0.52	0.40	1290	993	297	516
RCK	K	25	23.3	1	0.77	858	658	200	658
CK1	K	25	23.0	1	0.77	859	661	198	661

M_{binder} – Mass of binder; M_{cem} – Mass of cement; M_{ad} – Mass of addition; M_w – Mass of water

Cement pastes were prepared using a conventional multi-speed planetary mixer, where the dry solids were thoroughly mixed with water for approximately 8 min. The fresh pastes were then cast into 160 x 40 x 40 mm^3 prismatic moulds and covered with plastic film. For each composition, 18 prisms were produced to allow mechanical testing and morphological characterisation at different curing ages. After 12 h, three prisms per composition were demoulded. One half of a prism was sectioned into slices 4–5 mm thick, from which two slices were further fractured into 4 x 4 pieces, yielding specimens of approximately 1 cm^2. These samples were immediately immersed in isopropanol (C_3H_8O) to stop hydration. The isopropanol was replaced after 1, 3, 12, and 24 h, following the procedure described in [63]. Subsequently, specimens intended for SEM, N_2A, and MIP were oven-dried at 40 ºC for

24 h. Samples for XRD, TG, and NMR analyses were milled to a particle size below 125 μm and immersed in 50 mL of diethyl ether for 30 min, followed by oven-drying at 40 ºC for 30 min, as recommended in the literature [64]. All specimens were then vacuum sealed in plastic bags and stored in a desiccator until testing. The remaining prisms were demoulded after 24 h and cured in a controlled wet chamber (20 ± 2 ºC; RH > 90%) until testing at 1, 3, 7, 28, and 90 days. At each curing age up to 28 days, the same preparation procedure was applied to obtain specimens for morphological analysis.

2.3 Testing methods

Cement pastes were characterised in terms of mechanical strength, TG, XRD, NMR, SEM, MIP, and N_2A. Mechanical strength was determined according to EN 1015−11 [65] by measuring flexural and compressive strength at 1, 3, 7, 28, and 90 days. Flexural strength was first determined on prismatic specimens, followed by compressive strength testing on the resulting halves. Fresh pastes were further characterised for bulk density and consistency according to EN 1015-6 [66] and EN 1015-3 [62], respectively.

TG analyses were performed using a Hitachi Nexta STA under a nitrogen atmosphere. Approximately 15 mg of sample was heated from 20 ºC to 950 ºC at a rate of 15 ºC min^{-1}. In cement pastes, three main mass-loss regions are typically identified [67,68]: dehydration (L_{dh}), related to the loss of bound water from calcium silicate and aluminate hydrates; dehydroxylation (L_{dx}) of $Ca(OH)_2$; and decarbonation (L_{dc}). Although the exact temperature ranges depend on cement composition and testing conditions [68], in this study L_{dh}, L_{dx}, and L_{dc} were defined within 105–550 ºC, 400–450 ºC, and >550 ºC, respectively. Dehydration was considered above 105 ºC to exclude tightly bound adsorbed water, despite partial water loss from hydrates such as C–S–H and ettringite occurring below this temperature [46,68]. The L_{dx} contribution was quantified using the tangent method to correct for overlapping C–S–H mass loss [68], and L_{dh} was calculated as the mass loss between 105 and 550 ºC after subtracting L_{dx}. In clay–cement pastes, the mass losses from clay partially overlap L_{dh} and L_{dx} regions (Figure 5c). To account for this, corrections were made using the TG curve of the clay and its proportion in the mix. Basically, the correction is based on the following assumptions: the sample consists of hydrated cement and hydrated raw clay; the volume of anhydrous cement is three times that of the raw clay (25 vol.% cement replacement); the weight of anhydrous cement corresponds to the weight of the hydrated cement minus its mass loss up to 550 ºC; the mass loss of the blended sample

at a given temperature is considered to be the sum of the individual mass losses from the raw clay and the hydrated cement, weighted according to their respective proportions in the sample; the kaolin clay is not significantly attacked after cement hydration. In other words, L_{dh}, L_{dx}, and L_{dc} pertain only to the cementitious fraction, assuming that clay is inert. The same approach was applied to pastes containing quartz sand, whose mass losses are negligible (Figure 5d). Non-evaporable bound water (W_b) and portlandite content (CH) were calculated using Eq. (1)–(2), normalised to anhydrous cement weight at 550 ºC [46,68], with M_{CH}, M_{H_2O}, and M_{CO_2} denoting molecular weights of CH, H_2O, and CO_2, and $L_{dc,a}$ accounting for the carbonated material in anhydrous cement.

$$W_b = L_{dh} + L_{dx} + \frac{M_{H_2O}}{M_{CO_2}} \times \left(L_{dc} - L_{dc,a}\right) \quad (1)$$

$$CH = L_{dx} \times \frac{M_{CH}}{M_{H_2O}} + \frac{M_{CH}}{M_{CO_2}} \times \left(L_{dc} - L_{dc,a}\right) \quad (2)$$

XRD was performed using a Bragg–Brentano diffractometer (Bruker D8 Advance DaVinci, Karlsruhe, Germany) with Ni-filtered CuKα radiation operating at 40 mA and 40 kV. Data acquisition was obtained in the 2θ range 5-80 º, with a step size of 0.02 º, 0.5 s per step, and a spin rate of 15 rpm. Quantitative phase analysis was carried out via Rietveld refinement using the TOPAS 5.0 (Bruker AXS, Karlsruhe, Germany) software. Due to the complexity of the samples, which contained multiple phases from cement, clay, and their interactions, crystal structure parameters were not refined to avoid misleading results [69]. Moreover, the crystalline size parameter was omitted for minority phases (<1 wt.%). The fitting quality parameter Rwp was below 10% in all cases. To quantify the amorphous fraction, 10 wt.% zinc oxide (ZnO) was added and homogenized with 90 wt.% of the dried sample. Knowing the proportion of zinc oxide in the sample, the quantification of each phase was corrected using a factor based on the ratio between the measured and actual zinc oxide content The amorphous content was then determined as the difference between 100% and the sum of all quantified crystalline phases [70].

The consumption of anhydrous calcium silicates and the formation of C–S–H were investigated by NMR spectroscopy. Samples were packed in 4 mm zirconia rotors with Kel-F caps and analysed using a Bruker Avance III™ HD 500 MHz spectrometer (11.7 T magnetic field) equipped with a 4 mm CPMAS probe. The ^{27}Al magic-angle spinning (MAS)

NMR spectra were acquired at 130.3 MHz using 0.4 μs radio-frequency pulses, a recycle delay of 0.5 s, and a spinning rate of 12 kHz. Chemical shifts are reported relative to aqueous $Al(NO_3)_3$ set at 0 ppm. The ^{29}Si MAS NMR spectra were recorded at 99.3 MHz using 4.2 μs (45 º) pulses, a recycle delay of 30 s, and a spinning rate of 5 kHz, with chemical shifts referenced to tetramethylsilane (TMS).

The MIP measurements were performed using an AutoPore IV 9500 porosimeter (v1.09). Prior to testing, specimens were oven-dried under vacuum at 40 ºC for 24 h. Approximately 0.5–1.5 g of each sample was placed in the penetrometer, evacuated to ~50 mmHg in the low-pressure chamber, and intruded with mercury up to 0.21 MPa. The penetrometer was then transferred to the high-pressure chamber, where mercury pressure was increased in auto-speed mode up to 227.5 MPa with an equilibrium time of 40 s. Pore size distribution was calculated using Washburn's equation (Eq. 3), assuming a mercury surface tension (γ) of 0.485 N m^{-1} at 20 ºC and an advancing/receding contact angle (θ) of 130 º, corresponding to a pore diameter range of 0.006–330 μm.

$$d = \frac{4\gamma \times \theta}{p} \quad (3)$$

Nitrogen adsorption (N_2A) tests were conducted using a *Micromeritics ASAP 2010* analyser (*Micromeritics Instrument Corporation*) at 77 K, over a relative pressure range (P/P_0) of approximately 0.01–0.99, enabling the assessment of pore diameters in the range of ~2-150 nm. Approximately 1 g sample was degassed under vacuum at 40 ºC for 24 h prior to testing. The SSA and pore size distribution were determined using the BET multilayer adsorption and BJH methods, respectively [71]. In addition, the mean pore diameter (d_m), defined as four times the maximum pore volume divided by the SSA, was calculated. This approach is particularly suitable for characterising fine mesoporosity (2–50 nm), because condensation pressures vary minimally for pores larger than ≈100–200 nm, and maintaining high P/P_0 values is experimentally challenging [72].

Finally, the fracture surfaces of ≈ 1 cm^3 specimens were examined by SEM using a *Thermo Scientific Phenom ProX* equipped with an energy-dispersive X-ray spectroscopy (EDS) system. Prior to imaging, each sample surface was partially coated with an Au–Pd alloy using a dedicated mask, leaving approximately half of the surface uncoated. The coated area enabled high-quality SEM imaging by minimizing charge accumulation, while the

uncoated region was used for EDS elemental analysis to avoid inaccuracies associated with the presence of external elements introduced by the coating alloy.

3. Results and Discussion

3.1 Thermogravimetry analysis

Consistent with prior studies [46,73], RC had a high rehydration capacity, generating hydration products comparable to those of PC since the early stages of hydration (Figure 5a,b). The primary difference was the formation of AFm phases (calcium monosulfoaluminate) in RC within the first hours of hydration, as shown by the shoulder at 140−160 ºC in the derivative thermogravimetric (DTG) curves (Figure 5). This behaviour is attributed to the immediate rehydration of dehydrated AFm phases originally present in anhydrous RC [44,46]. In contrast, AFm phases in PC pastes were formed only after 3–7 days, depending on the paste composition. Ettringite initially forms and subsequently transforms into AFm phases as sulphates are progressively depleted. In this context, AFm formed more slowly in PC pastes without additions than in those containing additions (Figure 5a,c). This behaviour can be attributed to the slower sulphate depletion in pastes with higher cement and gypsum contents at the same w/c. In addition, cement hydration proceeds more rapidly at higher w/c due to increased water availability [74,75]. Accordingly, AFm phases developed earlier in CK1, which exhibited a higher w/c and lower solids content than CK (Figure 5c,e).

The evolution of W_b, L_{dh}, and CH for each paste is summarized in Table 3. All values were normalised to the anhydrous cement content and corrected to account for cement dilution in blended mixtures containing additions. Regardless of the cement type or the presence of additions, these parameters increased overtime, confirming the normal progression of hydration reactions.

At similar workability, RC pastes exhibited higher L_{dh} and W_b than PC pastes at all ages. This can be partly attributed to the higher w/c of RC pastes [45], which is known to accelerate hydration kinetics [75,76]. However, even at identical w/c, W_b remained higher in RCK than in CK1, particularly at early ages, up to 7 days. The larger SSA and higher solubility of RC likely promoted faster reactivity [76,77], confirming its high hydraulicity. By 28 days, however, the difference in W_b became negligible. This convergence can be partially explained by the higher CH content measured in CK1 compared with RCK after

12 h (Table 3; Figure 5e,f). The same was observed by Bogas et al. [46], who attributed this behaviour to the greater formation of CH from C_3S in PC, which is absent in RC, and to the higher proportion of carbonated CH in anhydrous RC. In addition, a more rapid formation of C–S–H in RC between 1 and 3 days was confirmed (Table 3; Figure 5b), which was identified as the period of most significant dissolution of α'_H−C_2S [46].

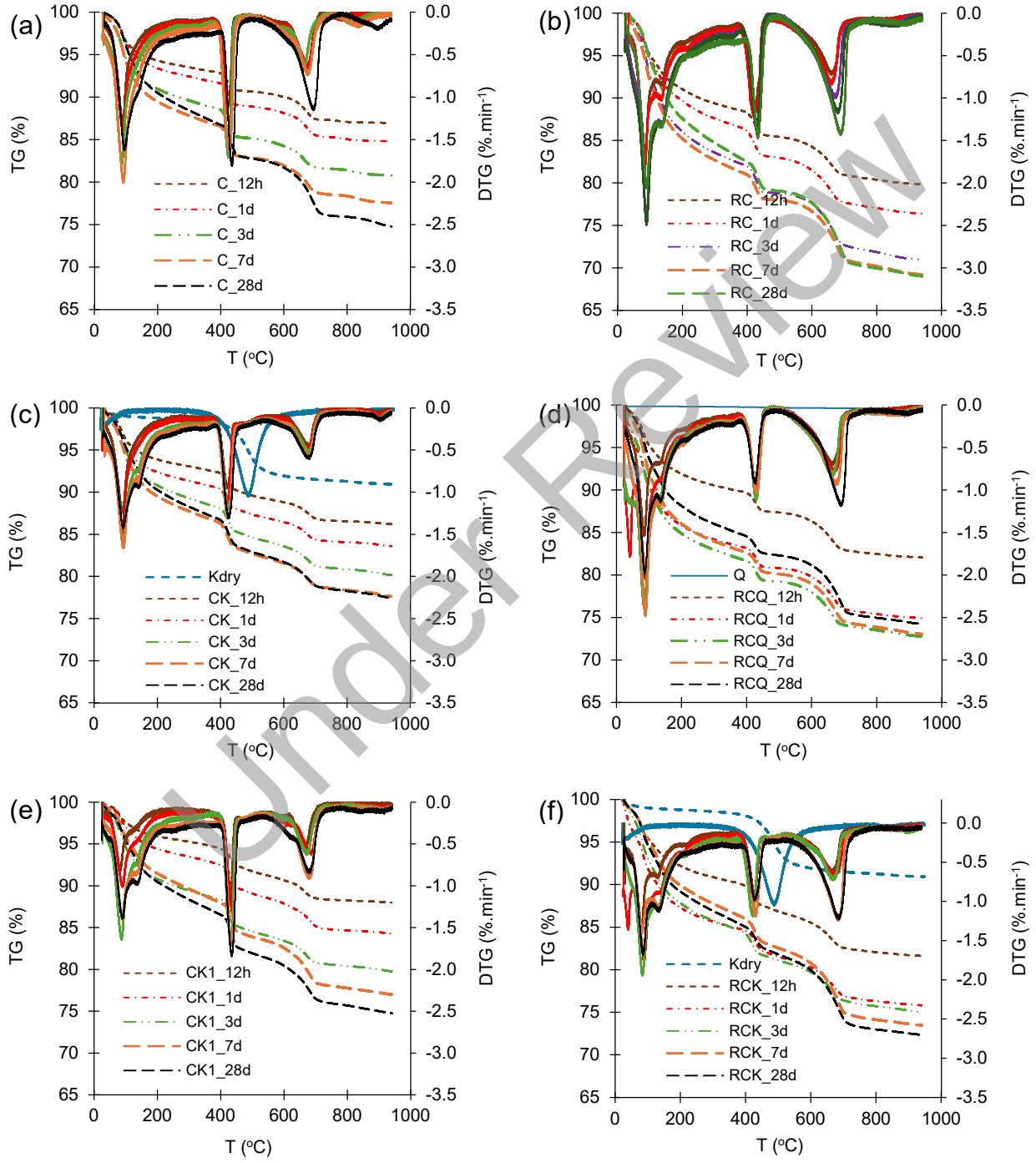

Figure 5 – Thermogravimetric (TG) and derivative thermogravimetric (DTG) curves of: (a) C; (b) RC; (c) CK; (d) RCQ; (e) CK1; (f) RCK.

In addition, weight losses associated with decarbonation (>550 ºC) were higher in RC pastes, reflecting the larger amount of carbonated compounds in anhydrous RC derived from cement waste (Figure 5). Furthermore, decarbonation related mass losses increased with curing age, which is likely associated with specimen preparation prior to testing [45,68].

Table 3 – Mass loss associated with the release of bound water from calcium silicate and aluminate hydrates (L_{dh}), amount of non-evaporable bound water (W_b) and portlandite content (CH) between 12 hours and 28 days, normalised to anhydrous cement fraction.

Mix	12 h			1 day			3 days			7 days			28 days		
	L_{dh} (%)	W_b (%)	CH (%)	L_{dh} (%)	W_b (%)	CH (%)	L_{dh} (%)	W_b (%)	CH (%)	L_{dh} (%)	W_b (%)	CH (%)	L_{dh} (%)	W_b (%)	CH (%)
C	4.5	7.2	10.9	5.8	9.1	13.7	7.8	12.1	17.9	9.8	15.0	21.4	12.2	18.7	26.8
CQ	4.6	7.3	11.3	7.0	11.0	16.3	10.0	14.8	19.6	12.0	17.6	22.8	14.8	20.7	24.5
CK	5.4	8.4	12.2	7.0	10.7	15.3	10.5	15.1	18.9	12.9	18.0	21.0	14.7	20.2	22.5
CK1	4.7	7.5	11.7	6.9	11.4	18.2	9.7	15.2	22.6	12.7	19.5	27.7	15.0	22.7	31.6
RC	8.5	12.0	14.4	11.0	15.4	18.3	14.2	19.5	21.6	14.6	20.3	23.4	16.2	22.6	26.2
RCQ	9.2	13.0	15.3	12.2	17.1	20.2	14.8	10.2	22.1	16.0	21.6	22.8	16.2	21.8	23.1
RCK	8.6	12.1	14.4	11.7	16.0	17.4	14.2	18.9	19.4	15.7	21.8	24.8	16.2	22.5	26.0

Contrary to previous studies [16,25], the partial replacement of cement with 25 % clay did not delay the early hydration of either PC or RC. On the contrary, an acceleration effect was observed in PC pastes, as evidenced by higher W_b and L_{dh} values (e.g., CK vs. C, Table 3). This effect can be primarily attributed to the filler and nucleation effects of kaolinite, whose high SSA provides additional sites for hydration products growth [10,24]. At a constant w/c, replacing cement with mineral additions reduces the effective w/b ratio and increases the solids fraction. Consequently, if the additions participate in hydration, the reduced water availability and available space for crystal growth may restrict the degree of hydration [76,78]. Therefore, nucleation effects are likely the dominant mechanism governing the enhanced hydration observed in blended systems. Accordingly, both RCQ and CQ exhibited a higher degree of hydration up to 28 days compared with RC and C, respectively. However, despite the higher hydration degree of the cementitious fraction in theses mixtures, non-blended pastes produced a larger absolute amount of hydration products when values were not normalised to cement content. The partial substitution of cement and the consequent clinker dilution limit the total formation of hydration products, as illustrated in Figure 5a–d. Nevertheless, when comparing CQ with CK or RCQ with RCK at equal w/c, no detrimental effect of the non-expanding clay on hydration evolution was observed.

The slight delay in hydration observed in CK1 in comparison with CK at 12 h can be attributed to its higher w/b, which is known to extend setting and delay the acceleration stage of hydration [79,80].

Several authors have proposed the occurrence of pozzolanic reactions between clay and cement. Liu et al. [24] suggested that C−A−S−H gel may form on clay surfaces due to the presence of unreacted Al–O or Si–O bonds. In the present study, the estimated CH content was slightly lower in CK than in CQ after 1 day, which may indicate partial CH consumption through clay–cement interactions (Table 3). However, this reduction was not systematically accompanied by a corresponding increase in C–S–H or C–A–S–H (L_{dh}). Moreover, a similar trend was not observed in RC pastes after 3 days. In addition, the relative L_{dh} content in CK compared with C decreased after 7 days, suggesting that nucleation effects rather than pozzolanic reactivity predominated. The gradual increase in CH observed over time in both CK and CK1 further supports the conclusion that significant pozzolanic reactions did not develop. Therefore, overall, these results indicate that physical effects dominate over potential chemical interactions between clay and cement. Nevertheless, after 3 days, CK exhibited a higher L_{dh}/CH ratio than the other mixtures, which may suggest limited clay–cement interactions. These interactions appear to be confined to minor surface reactions, as further discussed in sections 3.3 and 3.6. This behaviour was not observed in CK1, which had a higher w/c.

In RC pastes, the incorporation of clay had little influence on W_b, L_{dh}, and CH when compared with RC and RCQ. Both RCQ and RCK showed only a slight acceleration in hydration during the first day, with the most pronounced increase occurring after 12 h rather than between 1 and 3 days (Figure 5b,c,f; Table 3). Beyond 1-day, similar type and amounts of hydration products developed per unit volume of RC, suggesting a reduced influence of additions in this system. This behaviour can be attributed to the inherently high solubility and large surface area of RC, which likely diminish the contribution of additional nucleation effects. As further discussed in section 3.6, RC may also promote the formation of larger clay aggregates, thereby reducing the clay surface area and, consequently, its nucleation potential and interaction with RC. These results suggest that clay disperses more effectively in PC pastes than in RC pastes. Nonetheless, the low pozzolanic reactivity of the clay is confirmed, as shown in Figure 4.

Finally, the DTG curves of pastes containing quartz or clay were generally similar for both PC and RC systems. Notably, the ettringite-related peak in RCQ was more pronounced than in RCK, indicating a higher content of this phase (Figure 5d,f).

3.2 X-ray diffraction (XRD)

The main crystalline phases present in cement pastes containing kaolinite (K) or quartz (Q) additions are identified in Figure 6a−d. Owing to quartz's high crystallinity, its diffraction peaks dominated the diffractograms, hindering the visual identification of the other phases.

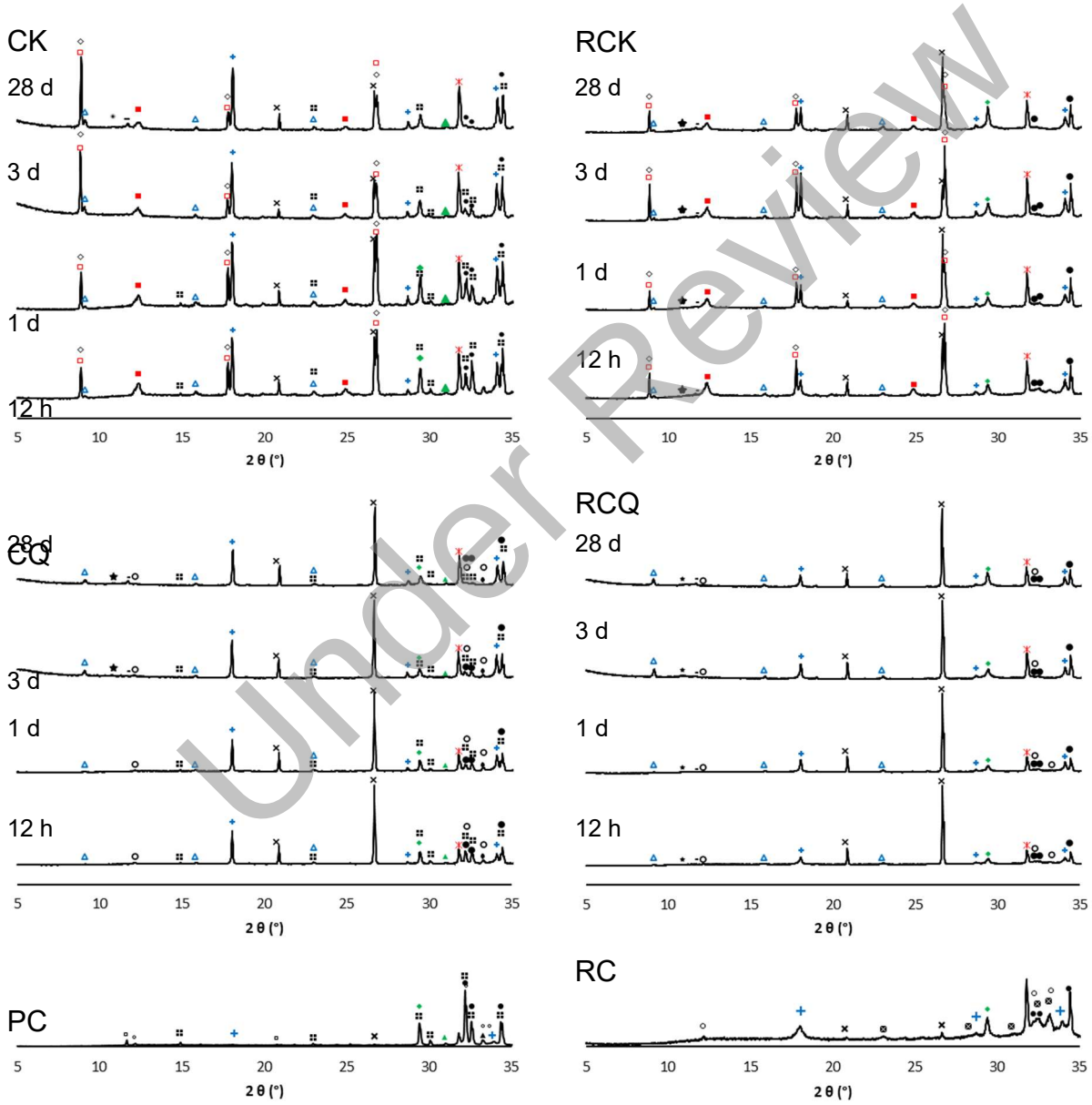

Figure 6 – X-ray diffraction analysis of: a) CK; b) RCK; c) CQ; d) RCQ; e) anhydrous PC; f) anhydrous RC.

As discussed in previous studies [46,73], the predominant anhydrous phase identified in RC pastes was the α′$_H$−C_2S polymorph, whereas PC pastes mainly contained C_3S and β−C_2S (Figure 6). In addition, unlike PC, anhydrous RC exhibited a high CH content, which can be attributed to the rapid rehydration of free CaO generated during the thermoactivation of cement paste waste [38]. The higher calcite content observed in RC pastes was consistent with the TG results and can be explained by the prior natural exposure of the precursor cement paste.

The evolution of the main anhydrous crystalline phases and the amorphous content over time, determined by Rietveld refinement (section 2.3), is presented in Figure 7. Results for the hydrated pastes were normalised to the anhydrous cement mass, accounting for loss of bound water, and to the cementitious fraction alone, excluding contributions from kaolinite and quartz. This normalization enables a more meaningful comparison of hydration behaviour across the different compositions. The amorphous content was quantified using 10 wt.% crystalline ZnO as an external standard. The accuracy of this estimation depends on the dispersion efficiency of ZnO, in addition to the intrinsic uncertainties associated with the Rietveld refinement method. The detailed phase evolution, expressed per unit of anhydrous mass and relative to the cement content, is reported in Table 4 and Table 5, together with the ICDD files used in the Rietveld refinement.

In RC pastes, a progressive consumption of α′$_H$−C_2S was observed throughout hydration, confirming its high reactivity and rehydration capacity, regardless of the presence of clay minerals in the mixture (Figure 6 and Figure 7). In blended RC pastes, α′$_H$−C_2S reacted significantly as early as 12 h, instead of only after 1 day as reported in [46]. This indicates an acceleration effect induced by kaolinite or quartz, in agreement with the TG results. As expected, *β*−C_2S had limited hydration up to 3 days in both RC and PC pastes (Figure 7).

AFm phases are poorly crystalline and therefore difficult to detect by XRD. They contributed to the high amorphous content observed in RC pastes from 12 h onward (Figure 7). In

contrast to PC pastes, RC pastes exhibited the formation of AFm phases as early as 12 h, mainly in the form of carboaluminates (Table 4 and Table 5). This behaviour was also reported in the literature [44,46] and is consistent with the TG results (section 3.1). Moreover, as also evidenced by TG analysis: i) ettringite formed in both RC and PC pastes, regardless of the type of addition (K or Q) and ii) RCQ developed a higher AFt content than RCK. Monosulfoaluminate phases were not detected, likely due to their low abundance and the dominance of more highly crystalline phases.

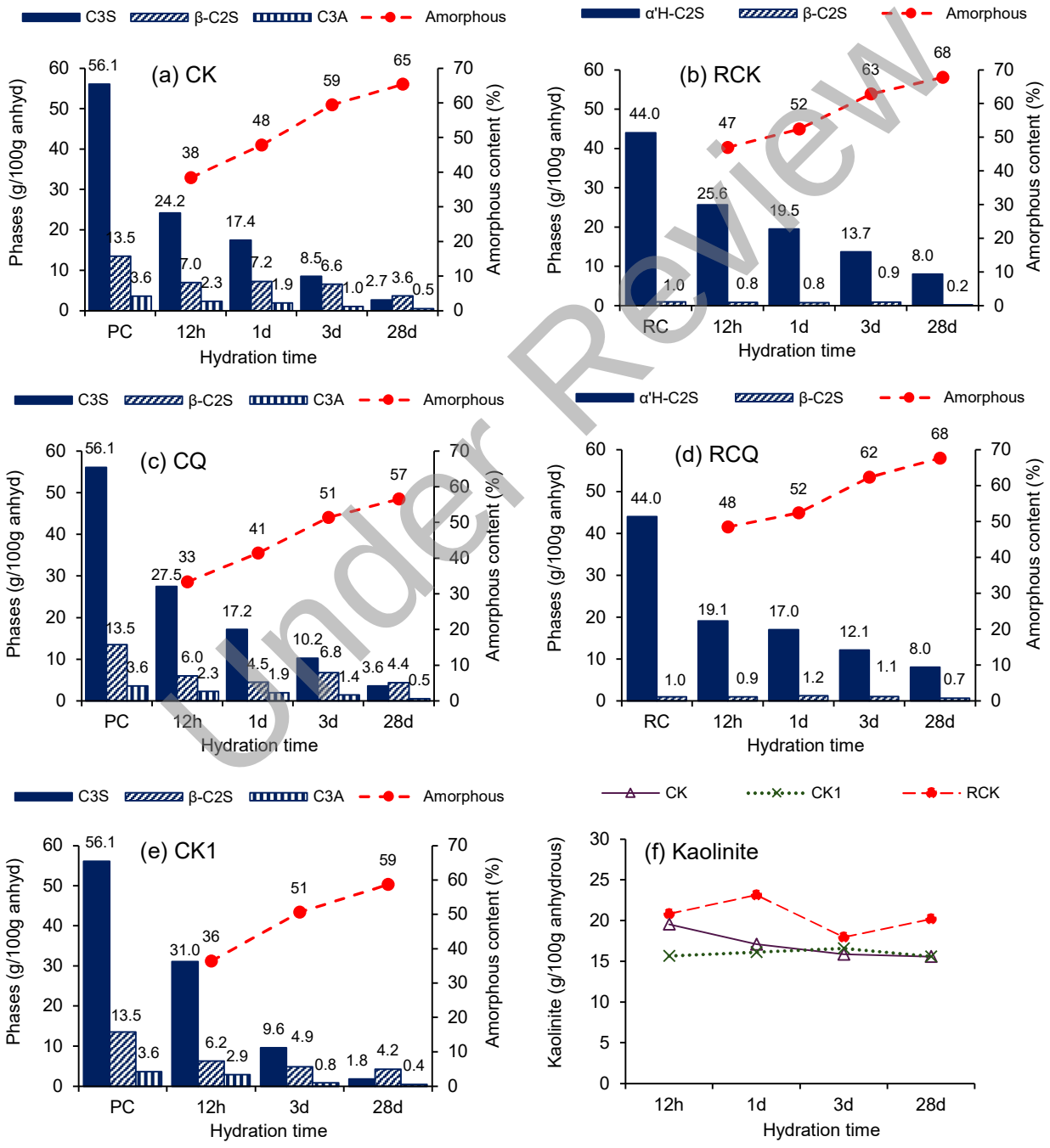

Figure 7 – Phase evolution and amorphous content of cement pastes over time (12 h to 28 days), determined by XRD Rietveld refinement: (a) CK; (b) RCK; (c) CQ; (d) RCQ; (e) CK1; (f) kaolinite.

Table 4 – Main crystalline phases in blended PC pastes from 12 h to 28 days, determined by Rietveld refinement and normalised to the anhydrous cement fraction.

Phases	ICDD	PC	CK				CK1			CQ			
			12 h	1 d	3 d	28 d	12 h	3 d	28 d	12 h	1 d	3 d	28 d
α'_H−C_2S	04-012-6734	NI	NI	NI	NI	NI	NI	NI	NI	NI	NI	NI	NI
β−C_2S	00-033-0302	13.5	7.0	7.2	6.6	3.7	6.2	4.9	4.2	6.0	4.5	6.8	4.4
C_3S	04-018-9701	56.1	24.2	17.4	8.5	2.7	31.0	9.6	1.8	27.5	17.2	10.2	3.6
C_3A	04-008-8069	3.6	2.3	1.9	1.0	0.5	2.9	0.8	0.4	2.3	1.9	1.4	0.5
C_4AF	04-006-8923	10.0	10.2	9.5	9.2	6.3	11.3	7.1	5.4	9.8	10.6	9.7	7.6
Calcite	00-005-0586	4.5	5.6	7.0	5.6	7.1	7.6	9.9	6.5	6.6	8.2	6.2	7.4
AFt	00-041-1451	NI	4.6	4.6	4.4	4.0	2.4	7.1	8.5	5.0	6.3	6.9	6.7
CH	00-004-0733	0.3	9.8	10.2	13.2	14.3	8.4	16.2	17.4	6.9	10.7	13.3	14.4
AFm−Mc	04-011-4223	NI	NI	NI	NI	5.2	NI	1.3	8.1	NI	NI	0.4	2.9
AFm−Hc	04-018-0025	NI	NI	NI	NI	1.3	NI	NI	NI	NI	NI	0.6	0.2

AFt: ettringite; CH: portlandite; AFm-Mc: calcium monocarboaluminate hydrate; AFm-Hc: calcium hemicarboaluminate hydrate; NI: non identified phase

Table 5 – Main crystalline phases in blended RC pastes from 12 h to 28 days, determined by Rietveld refinement and normalised to the anhydrous cement fraction.

Phases	ICDD	RC	RCK				RCQ			
			12 h	1 d	3 d	28 d	12 h	1 d	3 d	28 d
α'_H−C_2S	04-012-6734	44.0	25.6	19.8	13.7	8.0	19.1	17.0	12.1	8.0
β−C_2S	00-033-0302	1.0	0.8	0.8	0.9	0.2	0.9	1.2	1.1	0.7
C_3S	04-018-9701	NI	NI	NI	NI	NI	NI	NI	NI	NI
C_3A	04-008-8069	NI	NI	NI	NI	NI	NI	NI	NI	NI
C_4AF	04-006-8923	2.8	NI	NI	NI	NI	2.9	4.4	1.2	1.2
Calcite	00-005-0586	9.6	7.0	6.4	5.6	11.1	7.4	6.2	7.7	11.4
AFt	00-041-1451	NI	2.9	3.5	3.2	2.6	4.9	6.0	6.7	6.5
CH	00-004-0733	11.9	12.7	11.9	12.1	7.8	13.4	12.2	11.6	9.1
AFm−Mc	04-011-4223	NI	3.9	3.7	5.2	4.5	2.8	2.6	3.8	5.4
AFm−Hc	04-018-0025	NI	1.0	1.8	2.7	1.3	1.1	2.1	2.4	1.4

AFt: ettringite; CH: portlandite; AFm-Mc: calcium monocarboaluminate hydrate; AFm-Hc: calcium hemicarboaluminate hydrate; NI: non identified phase

A consistent trend in CH evolution was not always observed, particularly in RC pastes. Unlike the TG results, the values reported in Table 4 and Table 5 were not corrected for carbonation. In fact, part of the CH formed is likely to have carbonated, as reflected by the corresponding increase in calcite content.

The long-term volume of hydration products in RC pastes was slightly higher than that in PC pastes. This difference, also observed in the TG analysis (section 3.1), cannot be attributed solely to differences in w/c, as CK1 exhibited a lower amorphous content than both RCK and CK. However, CK1 showed a greater consumption of C_3S and a higher formation of AFt compared with CK.

The degree of reaction of the main phases in PC and RC pastes at 28 days (C_3S and α'_H-C_2S, respectively) was estimated relative to their original contents in the anhydrous materials. The degree of reaction of C_3S and α'_H-C_2S was around 0.94 and 0.82 in PC and RC pastes, respectively . Although C_3S was consumed to a greater extent in PC pastes, a substantial fraction of $\beta-C_2S$ remained unhydrated. As previously noted, RC pastes exhibited a higher amorphous content and a more rapid formation of AFm phases from the very early hours of hydration [45]. Once again, the pronounced consumption of α'_H-C_2S after 12 h of hydration is evident.

Notably, the degree of hydration of C_3S and α'_H-C_2S was similar in pastes containing either quartz or kaolinite, indicating that the clay had little influence on the hydration kinetics. Indeed, consistent with TG results, RC pastes with quartz or kaolinite showed similar hydration levels and evolution (Figure 7). At 28 days, both the residual α'_H-C_2S content and the amorphous fraction were equivalent in both RC pastes. However, PC pastes containing kaolinite showed a slight increase in hydration and C_3S consumption compared with pastes with the same amount of quartz. This effect was already evident at early ages and, as discussed in section 3.1, supports an enhanced filler and nucleation effect of kaolinite.

It is nevertheless valuable to assess whether there is a chemical interaction between the cement and kaolinite. Figure 7f shows the evolution of the crystalline kaolinite content over time, as estimated by Rietveld refinement. Despite the variability inherent to the method, CK shows a slight trend of kaolinite consumption over time. However, the consumption rate diminished progressively, suggesting a surface-limited phenomena (Figure 7). In contrast,

no clear reduction in kaolinite content was observed in RCK or in CK1, indicating that cement–clay interactions may be favoured in systems with lower w/c.

However, Feng et al. [80] reported enhanced pozzolanic reactivity in LC^3 pastes with increasing w/b (0.3–2.0), which was attributed to greater water availability and space in interparticle regions. Similar observations were made by Hay and Celik [79] for LC^3 pastes with w/b ratios between 0.25 and 0.6. Nevertheless, in the present study, a higher participation of reactive species likely occurred in CK compared with CK1, possibly due to more effective dispersion of kaolinite in PC pastes with lower w/b. In addition, higher w/b ratios are associated with greater CH dilution and higher pore saturation [79], which may slow down pozzolanic reactions. The potential interactions between cement and the kaolinite surface will be further discussed in sections 3.3 and 3.6.

3.3 Nuclear magnetic resonance (NMR)

The solid-state NMR spectroscopy provides detailed information on the arrangement of SiO_4 tetrahedra in solid silicates, enabling the identification of $Q^n(mAl)$ species, where *n* represents the total number of bridging oxygens linking adjacent tetrahedral units, of which *m* are connected to Al atoms [81,82]. Accordingly, the degree of silicate chain polymerisation increases with increasing *n*. In common cementitious systems, Q^0 species correspond to isolated anhydrous calcium silicate phases (C_2S and C_3S), whereas Q^1 and Q^2 represent end-chain and middle-chain units, respectively. Q^3 species, associated with branching sites, may develop in cements containing pozzolanic additions or in C–S–H with low Ca/Si ratios, while Q^4 denotes fully polymerized silica in a three-dimensional framework [83], such as that present in the quartz used in RCQ and CQ mixtures.

The ^{29}Si and ^{27}Al solid-state NMR spectra of pastes at 28 days are shown in Figure 8. The deconvoluted Q^n sites obtained from the ^{29}Si NMR spectra were integrated to estimate the quantitative parameters defined by Eq. (4)–(6), namely the mean chain length (M_{CL}) of C–S–H, the degree of hydration (α_{NMR}), and the $Al_{(IV)}$/Si ratio, where applicable [82,84–86]. As only Q^0 to Q^2 species were newly formed in the hydrated cement pastes, Eq. (4)–(6) are presented without inclusion of Q^3 groups. Deconvolution of the ^{27}Al NMR spectra was not performed due to the overlap of multiple Al-bearing phases and the resulting insufficient fitting accuracy. Nevertheless, the ^{27}Al NMR provides qualitative insight into the incorporation of Al into C–S–H, as a result of potential clay–cement interactions [87].

$$M_{CL} = \frac{2Q^1 + 2Q^2 + 3Q^2(1Al)}{Q^1} \quad (4)$$

$$\alpha_{NMR} = \frac{Q^1 + Q^2}{Q^0 + Q^1 + Q^2} \quad (5)$$

$$\frac{Al_{(IV)}}{Si} = \frac{0.5\ Q^2(1Al)}{Q^1 + Q^2 + Q^2(1Al)} \quad (6)$$

The clay used in this study consists primarily of kaolinite, a 1:1 layered mineral composed of SiO_4 tetrahedral sheets and AlO_6 octahedral sheets, and mica-type clay, a dioctahedral 2:1 phyllosilicate in which an AlO_6 octahedral sheet is sandwiched between two SiO_4 tetrahedral sheets. In the ^{29}Si NMR spectra (Figure 8), resonances at approximately -91 ppm and -107 ppm are assigned to kaolinite and quartz, respectively [7,88,89]. Moreover, a broad contribution on the high-frequency side of the main resonance was observed. A similar feature was reported by Mantovani [89] as involving $Q^3(1Al)$ to $Q^3(3Al)$ species, associated with illite/muscovite structures. In these 2:1 phyllosilicates, isomorphic substitution of Si^{4+} by Al^{3+} occurs within the SiO_4 sheets, which are charge-balanced by interlayer K^+ [89]. The $Q^3(1Al)$ resonance is consistent with the chemical shift of approximately -86 ppm reported for muscovite [90], as also observed in Figure 7. In the ^{27}Al NMR spectra, two main signals were identified at ≈ 5 ppm and in the range of 60–80 ppm (Figure 8), corresponding to octahedrally coordinated $Al_{(VI)}$ and tetrahedrally coordinated $Al_{(IV)}$, respectively, which arises from Al−for−Si substitution in SiO_4 tetrahedra [88,89,91,92]. This confirms the presence of both kaolinite and mica-type clay minerals.

In the hydrated cement pastes, four deconvoluted ^{29}Si resonances in the range of -60 to -90 ppm were identified, corresponding to unreacted calcium silicates (Q^0) and C–S–H formed during hydration (Q^1 and Q^2). The associated ^{29}Si chemical shifts ($\delta^{29}Si$), together with the calculated M_{CL}, α_{NMR}, and $Al_{(IV)}/Si$ ratio are summarized in Table 6.

In PC pastes, the Q^0 resonances at ≈ -71 ppm and -74 ppm can be assigned to belite and alite, respectively [83,88,93]. As previously noted, anhydrous RC lacks C_3S, with α'_H-C_2S being the predominant phase. Consequently, RC pastes exhibited a new resonance near -70 ppm, slightly left of $\beta-C_2S$ (Figure 8), consistent with chemical shifts reported in earlier studies on RC [94] and within the documented range for $\alpha-$ and α'_L-C_2S (-70 to -71 ppm) [88,90]. The C_2S resonances tend to overlap making their precise individualisation difficult. As observed in XRD analysis, the amount of $\beta-C_2S$ in RC was low (section 3.2). In mature

pastes, isotropic chemical shifts around -79 ppm and -84 ppm are assigned to Q^1 [95,96] and Q^2 units [91,94], respectively.

Table 6 – ^{29}Si NMR data of PC and RC pastes at 28 days: isotropic chemical shifts ($\delta^{29}Si$), degree of hydration (α_{NMR}), C–S–H mean chain length (M_{CL}), and $Al_{(IV)}/Si$ ratio of C−S−H.

Composition	Peaks	ppm	Area	α_{NMR}	M_{CL}	$Al_{(IV)}/Si$
C	Q2 (0Al)	-83.65	1.9	0.66	2.99	0.004
	Q2 (1Al)	-81.5	0.05			
	Q1 (0Al)	-78.3	4			
	Q0	-73.75	0.63			
	Q0	-70.5	2.45			
CQ	Q2 (0Al)	-83.3	1.935	0.75	2.79	–
	Q1 (0Al)	-77.9	4.9			
	Q0	-73.55	0.6			
	Q0	-70.5	1.72			
CK	Q3	-90.75	2.3	0.81	2.94	0.033
	Q3 (1Al)	-86	1.2			
	Q2 (0Al)	-84.55	1.6			
	Q2 (1Al)	-81.7	0.45			
	Q1 (0Al)	-78.5	4.85			
	Q0	-74.3	0.11			
	Q0	-71	1.55			
CK1	Q3	-90.7	2.65	0.81	2.82	0.008
	Q3 (1Al)	-86.3	1.575			
	Q2 (0Al)	-83.5	1.9			
	Q2 (1Al)	-81.6	0.12			
	Q1 (0Al)	-79.1	5.05			
	Q0	-73.9	0.35			
	Q0	-70.9	1.3			
RC	Q2 (0Al)	-84	2.05	0.87	2.85	0.006
	Q2 (1Al)	-81.55	0.08			
	Q1 (0Al)	-78.45	5.13			
	Q0	-72.3	0.13			
	Q0	-70.4	1			
RCQ	Q2 (0Al)	-84.05	2.25	0.89	2.91	–
	Q1 (0Al)	-78.67	4.925			
	Q0	-72.6	0.4			
	Q0	-70.5	0.53			
RCK	Q3	-90.7	2.9	0.91	3.05	0.009
	Q3 (1Al)	-86.5	1.85			
	Q2 (0Al)	-84.2	2.37			
	Q2 (1Al)	-81.6	0.14			
	Q1 (0Al)	-79.06	4.9			
	Q0	-71.97	0.4			
	Q0	-69.15	0.33			

The high rehydration capacity of RC is confirmed from the substantial development of Q^1 and Q^2 units, regardless of the type of addition used. Moreover, the chemical shifts of these

Q units are similar to those observed in common cement pastes, indicating the formation of the same type of C–S–H. Compared with PC pastes of similar workability, RC pastes exhibited a higher α_{NMR}, primarily due to their higher w/c [45,97]. However, even comparing pastes with equal w/c, RCK showed slightly higher α_{NMR} and M_{CL} than CK1, consistent with the trends observed in sections 3.1, 3.2 and 3.7. In RC pastes, Q^0 species were largely depleted, and greater amounts of more polymerized C–S–H were formed. Similar behaviour has been reported in previous studies [46,94] being attributed to the higher surface area and faster reactivity of RC, as well as its lower β−C_2S content. In fact, consistent with section 3.2, C_3S and α′$_H$−C_2S underwent significant consumption, in contrast to β−C_2S [98].

As observed in section 3.1, the incorporation of quartz or kaolinite accelerated the hydration of both RC and PC pastes (Table 3), confirming their role as effective nucleation sites. This effect was particularly pronounced in PC pastes. Notably, pastes containing kaolinite exhibited slightly higher α_{NMR} and M_{CL} values than other mixes, including those with quartz additions. This subtle trend was not reflected in the TG results, which showed comparable hydration rates at 28 days for pastes containing either quartz or kaolinite.

The ^{29}Si NMR spectra of CK and RCK pastes were affected by the presence of clay Q^3 resonances, which partially overlapped Q^2 signals (Figure 8, Table 6). In addition, a shoulder at ≈-81.6 ppm occurred, which can be assigned to Q^2(1Al), reflecting the incorporation of Al into the C−S−H structure [7,82,99]. While this Al substitution may had originated from aluminate phases in the clinker, the prominence of this peak in CK suggests that clay contributed to the formation of C−A−S−H, which is consistent with the $Al_{(IV)}$/Si ratios in Table 6. The ^{27}Al NMR spectra showed a resonance between 60−80 ppm, confirming the presence of tetrahedrally coordinated $Al_{(IV)}$ replacing for Si in C−S−H. However, a similar hump was also observed in the raw clay, indicating that Al−for−Si substitutions were already present in its silica sheets.

Krøyer et al. [7] also reported an increased Q^2(1Al) content in hydrated PC pastes containing 20 % kaolinite. In that study, however, kaolinite was not significantly consumed during hydration, and the observed acceleration effect was attributed primarily to nucleation, which also promoted higher Q^2(0Al) content and M_{CL}. In the present study, only negligible changes in the position and intensity of clay-related Q^3 peaks were observed, indicating low kaolinite reactivity and no substantial consumption up to 28 days.

Nevertheless, despite the low integrated area of $Q^2(1Al)$, pastes containing clay exhibited a higher degree of hydration and greater chain length of C–S–H (M_{CL}), in both RC and PC systems. Therefore, the incorporation of clay promoted C–S–H formation, enhancing both its quantity and degree of polymerisation. Any clay–cement interaction is likely limited to surface effects, involving defective sites or partial edge dissolution, as further discussed in section 3.6. By providing a large surface area for nucleation, clay particles can also stimulate the incorporation of Al into the C–S–H structure.

The differences in M_{CL} and α_{NMR} between pastes containing quartz or clay were more pronounced in CK than in RCK (Table 6), consistent with TG and XRD results. In addition, the relative proportion of Q^3 to other Q^n species was slightly lower in CK (0.29) than in RCK (0.37), suggesting stronger clay–cement interactions in CK. This is supported by the estimated $Al_{(IV)}$/Si ratios, which were 0.033 for CK and 0.009 for RCK (Table 5). In CK1, the ratio was only 0.008, which corroborates the hypothesis that clay is better dispersed and interacts more effectively with cement in PC pastes of lower w/c.

Overall, the greater C–S–H formation observed in CK was attributed to both nucleation and cement–clay interaction effects. In RCK, these effects are less apparent, not only due to poorer clay dispersion but also because the high surface area of RC particles promoted enhanced C–S–H nucleation, masking potential clay–cement interactions. Nevertheless, given the comparable degrees of hydration related to C–S–H formation, as evidenced in sections 3.1−3.2, the reaction of CH with clay was likely minimal up to 28 days.

The 0–20 ppm region of the ^{27}Al NMR spectra was challenging to interpret (Figure 8), as multiple phases containing octahedrally coordinated Al(VI) have their shifts cluster, including ettringite (~13 ppm), monosulphates (~10−12 ppm), monocarboaluminates (~8−9 ppm), and other aluminate hydrate phases [81,82,88,93,99,100]. The spectra shows that PC pastes exhibited a more pronounced shoulder between 4 and 12 ppm than RC pastes, which could suggest greater AFm formation in PC. However, this was not corroborated by TG analysis (section 3.1). This region is also affected by unhydrated C_4AF (~8–10 ppm) [81,101–103], which was more abundant in PC pastes (Table 4). Nevertheless, obtaining a well-defined signal from Al in C_4AF was also challenging as it is significantly broadened due to the paramagnetic iron [102–104]. Additionally, the ^{27}Al NMR spectra of CK and RCK are also affected by the presence of clay in this region (~5 ppm, Figure 8).

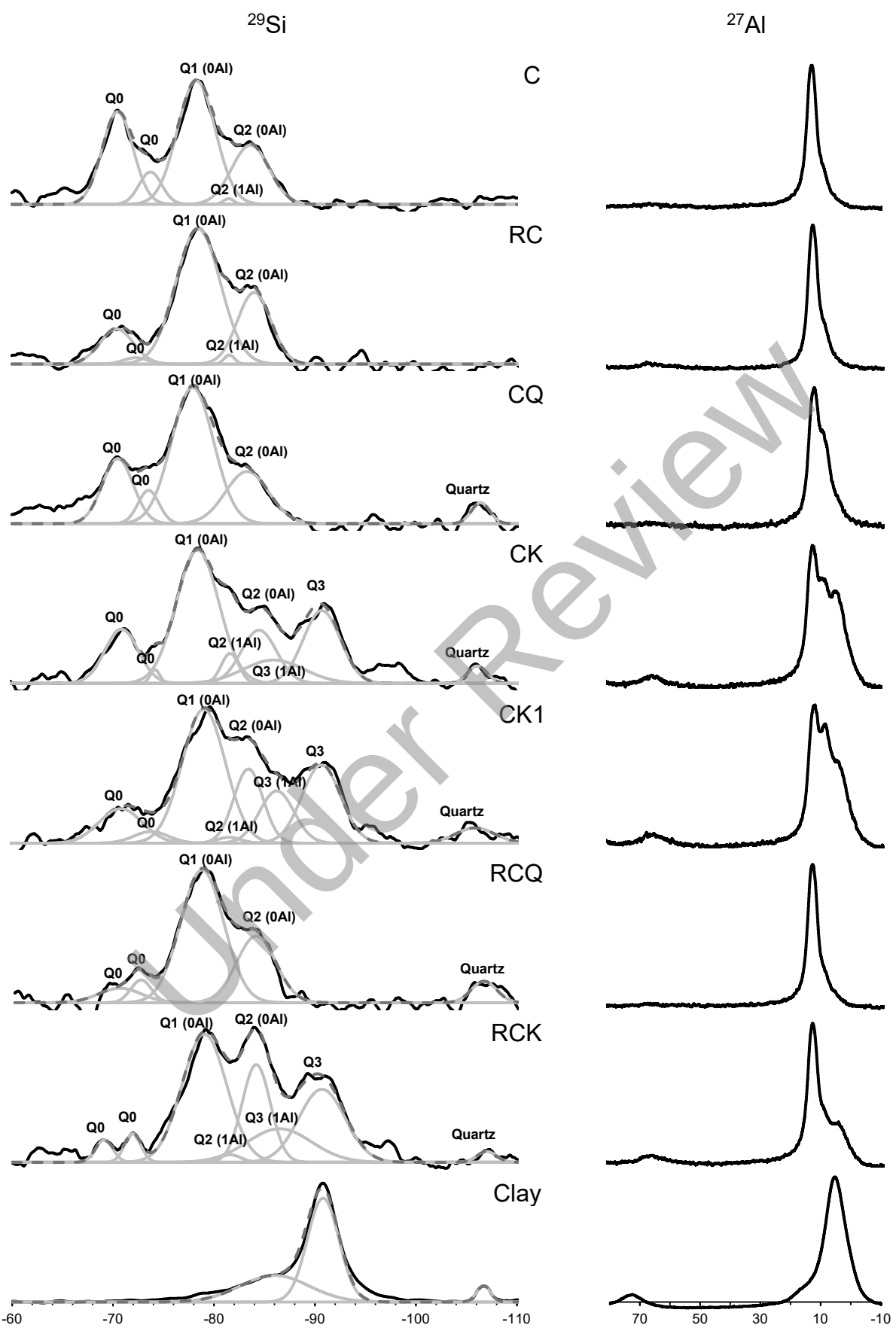

Figure 8 – ^{29}Si and ^{27}Al NMR spectra of RC and PC pastes at 28 days and kaolinite-rich clay.

3.4 Mercury intrusion porosimetry

The MIP porosity was primarily governed by the w/c, with RC pastes exhibiting higher total porosity and a coarser pore structure than PC pastes of comparable workability (Figure 9). For a given w/c, the incorporation of quartz or kaolinite led to a reduction in MIP porosity, contributing to a more refined microstructure, particularly in PC pastes.

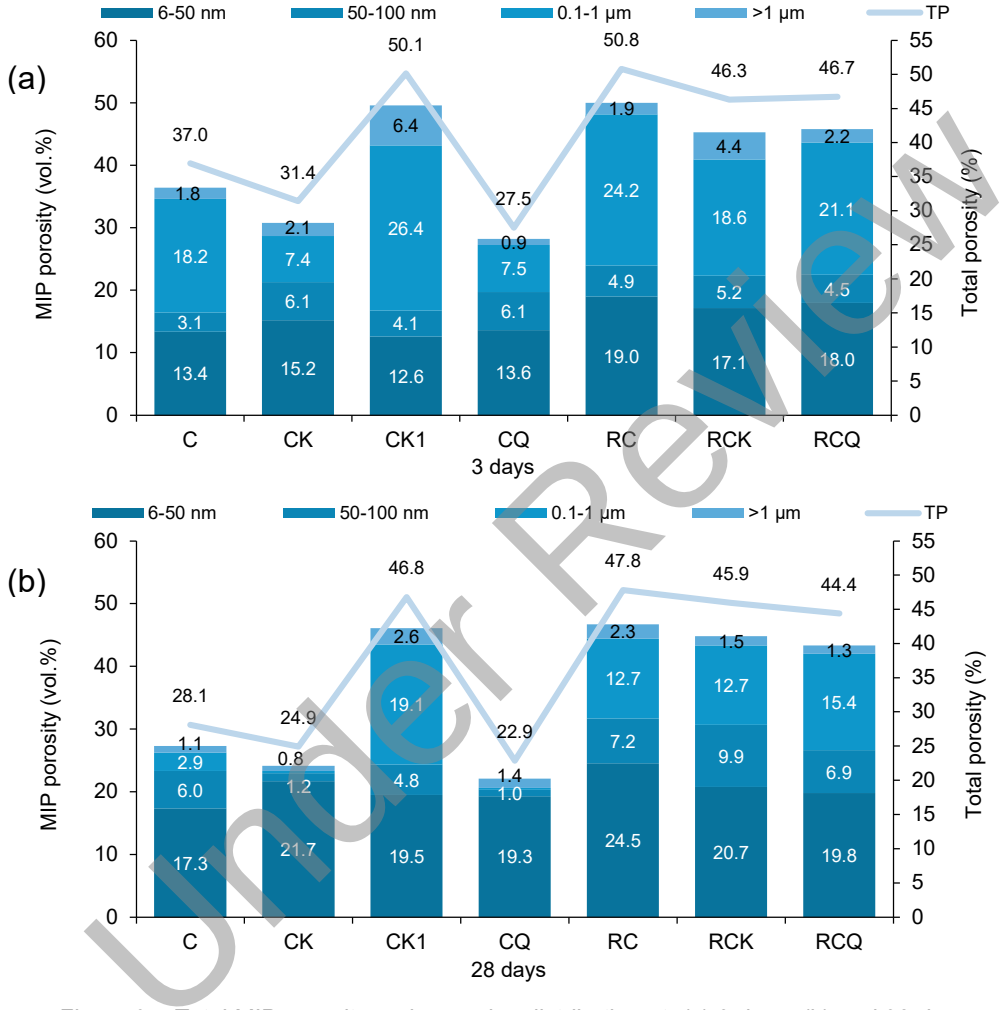

Figure 9 – Total MIP porosity and pore size distribution at: (a) 3 days; (b) and 28 days.

For the same w/c, RCK developed a slightly lower total MIP porosity than its PC counterpart CK1, particularly at early ages, corroborating the faster reactivity of RC observed in sections 3.1–3.3. Moreover, at similar total porosity, RCK developed a more refined pore structure, characterised by a higher proportion of mesopores (<100 nm) (Figure 9). This refinement is clearly observed in Figure 10, where the first peak corresponding to the critical pore diameter was approximately four times smaller in RCK than in CK1. A similar trend was reported by Bogas et al. [45]. This behaviour can be explained by the dual-peak pore

structure developed in RC pastes, associated with intra-particle porosity (within RC particles) and inter-particle porosity (between RC particles), as evidenced in Figure 10. As part of the mixing water was retained within the pores of RC particles, the effective inter-particle space was reduced, leading to a less coarse microstructure. This effect was more pronounced at early ages, when the difference between intra- and inter-particle porosity was greater due to the development of fewer hydration products (Figure 9). In contrast, PC pastes exhibit a different behaviour, with only interparticle porosity progressively decreasing over time.

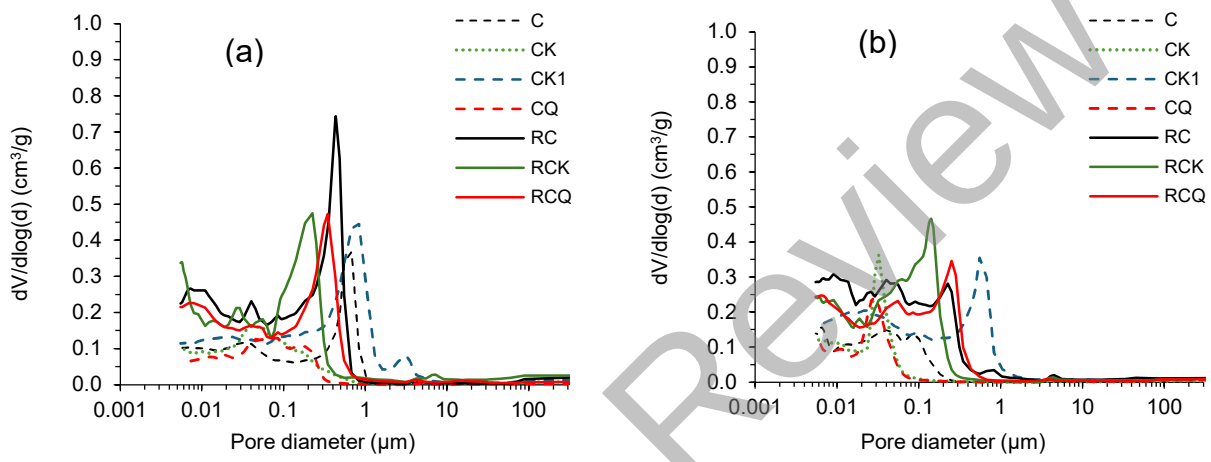

Figure 10 – Log differential MIP intrusion volume at: a) 3 days; b) and 28 days.

The reduction in total MIP porosity resulting from the partial replacement of cement with additions was partly related to differences in cement content for the same w/c. Although the pastes shared the same w/c, variations in the w/b meant that mixes without additions were produced with a higher effective water content, which contributed to their higher porosity. A similar analogy applies when comparing the porosity of mortars and pastes with the same w/c, as only the paste fraction contributes to the overall porosity. The incorporation of additions had a more pronounced influence on PC pastes than on RC pastes. Partial replacement of PC with fine quartz or clay reduced both the MIP porosity and the average pore diameter of pastes, particularly at early ages (Figure 10). This behaviour confirmed the filler and eventual nucleation effects of these additions, which enhanced matrix compactness and refined the pore structure. Accordingly, a marked reduction in the volume of coarse pores larger than 50 nm was observed in blended mixes (Figure 9). However, the microstructure of CK and CQ pastes were similar, confirming the low pozzolanic reactivity of the clay. In addition to differences in particle dispersion and the resulting compactness (section 3.7), the slightly higher MIP porosity of CK compared with CQ, particularly within

the fine mesopore range (<50 nm), can also be attributed to inter-particle porosity associated with clay clusters.

In RC pastes, the incorporation of quartz or clay had only a minor effect on the pore structure. As previously discussed in section 3.1, these additions had low influence on hydration, owing to the inherently high reactivity and large surface area of RC. It is also likely that the additions were less effectively dispersed in RC pastes, due to their higher water demand, poorer fluidity, and less available free water between particles. This will be further discussed in section 3.6.

The lower proportion of fine mesopores (<50 nm) observed in blended RC pastes (Figure 9) can be attributed to the dilution promoted on the volume of porous RC particles and hydrated products, for the same w/c. As in PC pastes, the relative proportion of fine mesopores in RCK compared with RCQ was influenced by the inter-particle porosity of clay agglomerates, whereas non-porous quartz particles did not contribute to MIP porosity. Nevertheless, as shown in Figure 10, the critical pore diameter was smaller in RCK than in RCQ, indicating slightly greater macropore refinement (0.1–1 μm). This effect was not observed in PC pastes.

From 3 to 28 days, a progressive refinement of the pore structure was observed for all paste compositions (Figure 9−Figure 10). This refinement was more pronounced in PC pastes than in RC pastes, even at the same w/c, owing to the higher early-age hydration rate of RC within the first 3 days. The type of addition had a negligible influence on the evolution of total porosity between 3 and 28 days, irrespective of the cement type.

3.5 Nitrogen adsorption (N_2 adsorption)

The SSA and average pore diameter (d_m), determined according to Eq.(3), are presented in Figure 11, while the corresponding pore size distributions are shown in Figure 12−Figure 13. Note that N_2 adsorption analysis is inaccurate for pores larger than 50 nm at relative pressures $P/P_0 > 0.96$ [105]. Nevertheless, in contrast to MIP, the pore size distributions derived from N_2 adsorption are less affected by the bottleneck effect, which overestimates the fraction of small pores [106,107].

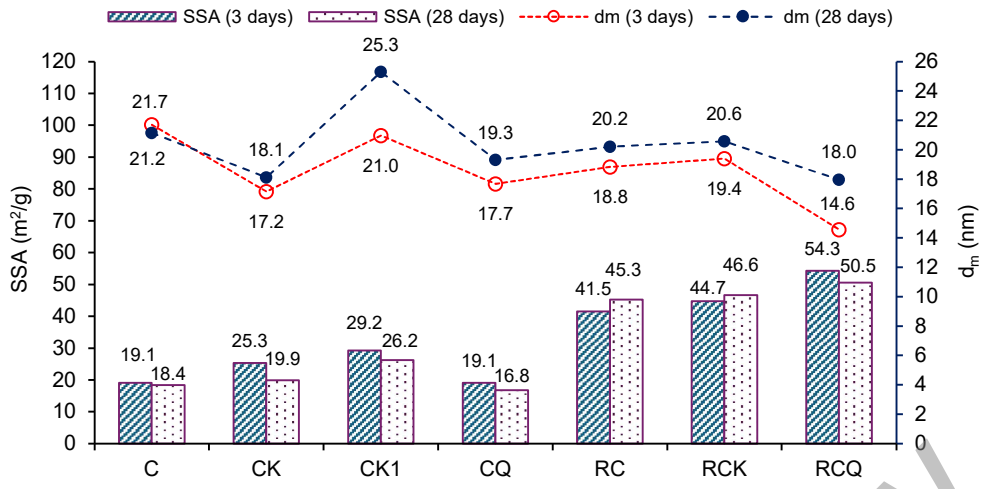

Figure 11 – Specific surface area (SSA) and mean pore diameter (d_m) from N_2 adsorption tests, at 3 and 28 days

As discussed in the literature [108,109], the total pore volume and SSA increased with w/c (CK vs CK1), which contributed to the pronounced differences observed between PC and RC pastes (Figure 11 and Figure 12). RC pastes, with a w/c twice that of PC pastes, exhibited a more open and loosely connected pore structure, with greater accessibility to small pores.

In pastes with high w/c, including CK1 and those containing RC, the volume of fine pores increased over time (Figure 11 and Figure 12), reflecting progressive refinement of the microstructure through the formation of hydration products with high SSA [108]. This behaviour demonstrated the continuous hydration of RC over time. In contrast, in low w/c pastes, SSA and pore volume decreased between 3 and 28 days (Figure 11 and Figure 12), as the available space became increasingly filled and blocked by hydration products, reducing pore connectivity [108,110]. Additionally, high w/c pastes are dominated by low-density C–S–H with high SSA [111].

The incorporation of RC increased the SSA and total pore volume, even in pastes with equal w/c (RCK vs CK1, Figure 11 and Figure 12). This effect can be explained by the porous nature and high surface area of RC, which increased the volume of small pores, particularly those below 50 nm (Figure 12). As mentioned, in addition to the RC porosity, the inter-particle porosity in RC pastes was more refined than in PC pastes of equal w/c. Furthermore, as discussed in sections 3.1 and 3.2, RC pastes developed higher contents of AFm phases from early ages, which are associated with higher SSA than ettringite [112]. In addition, the d_m was similar in RC and PC pastes of distinct w/c and slightly higher in

CK1 of equal w/c (Figure 11), highlighting the role of RC in effectively refining the microstructure.

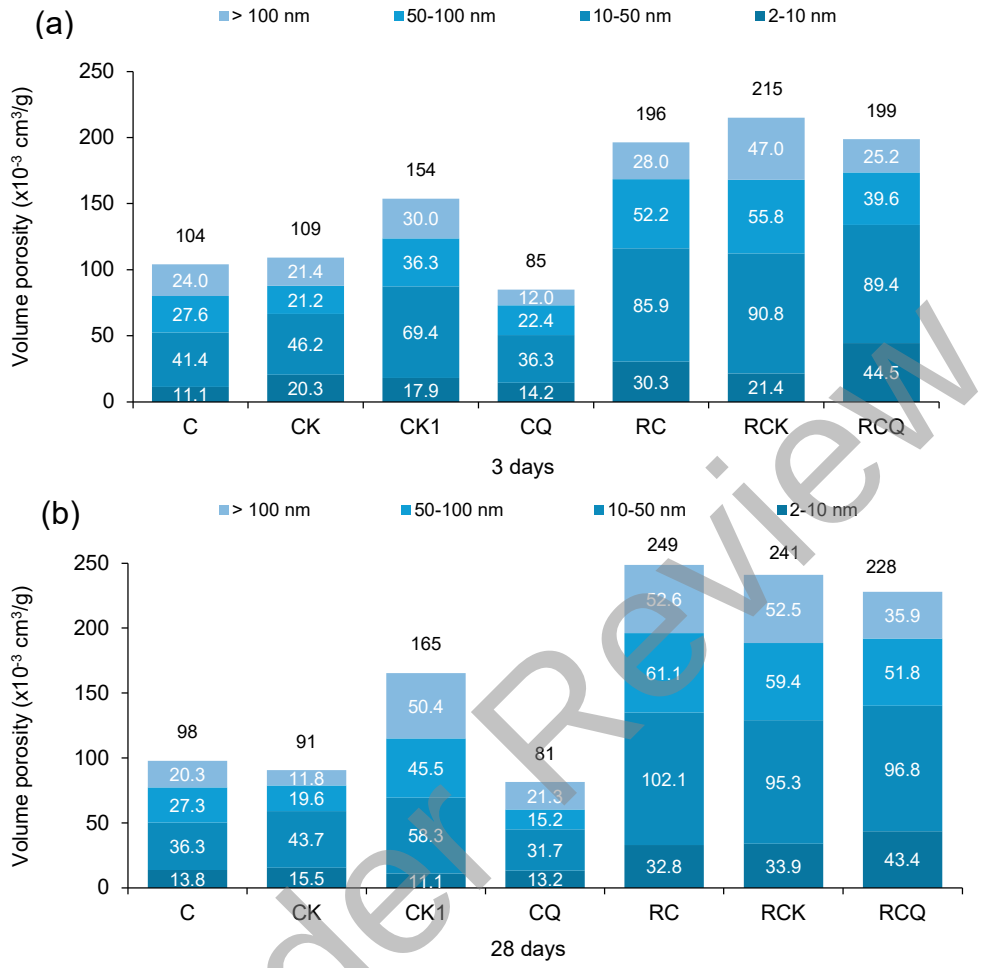

Figure 12 – Pore size distribution from N2 adsorption analysis, at: (a) 3 days; (b) and 28 days.

Only minor differences in SSA and porosity were observed after partially replacing cement with quartz or clay. Due to the higher cement content for the same w/c, pastes without additions would be expected to exhibit greater pore volume and higher SSA. However, blended pastes developed more hydration products per unit of cement (sections 3.1–3.3), particularly at early ages, which reversed this trend (Figure 12, 3 days).

The results confirmed the limited influence of the type of addition on microstructure development. Pore size distribution curves exhibited similar configuration in pastes containing quartz and clay (Figure 12). In PC pastes, the slightly higher pore volume and SSA in CK compared with CQ were primarily due to the porous nature and larger surface area of clay particles. The similar reduction in fine pores and corresponding pore refinement

observed in both mixtures between 3 and 28 days (Figure 13) confirmed their similar hydration behaviour and minimal clay-cement interaction.

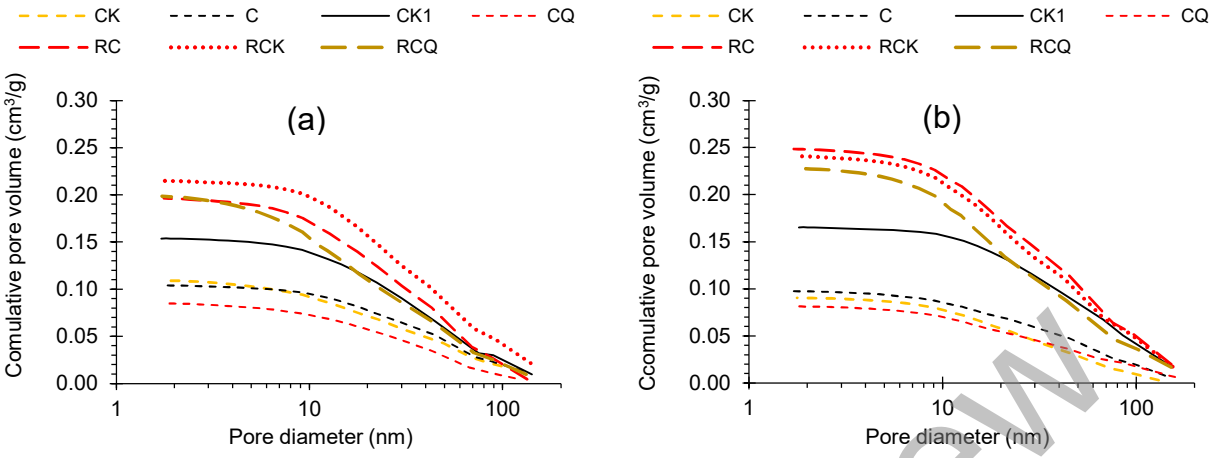

Figure 13 – Cumulative pore volume as a function of pore diameter at: (a) 3 days; (b) and 28 days.

In RC pastes, the little influence of the type of addition was also confirmed. However, RCQ exhibited a higher proportion of very fine pores, particularly at 3 days (Figure 12), consistent with its slightly higher hydration degree compared with RCK (section 3.1). Furthermore, as discussed in sections 3.1 and 3.2, greater ettringite formation was observed in RCQ compared to RCK, which acted as a space-filling phase while simultaneously increasing SSA and fine porosity. This likely explained the higher SSA and lower d_m in RCQ (Figure 11). At 28 days, the differences between mixes diminished, and the pore size distribution curves exhibited similar shapes (Figure 13).

The greater early hydration (section 3.1), higher proportion of fine pores, and larger SSA observed in CK compared to CQ (features not observed in RC pastes) further suggested that clay was more effectively dispersed in PC pastes.

3.6 Scanning electron microscopy (SEM)

SEM images indicates that the microstructure of the paste containing RC (RCK, Figure 14a,c) was denser than that of the PC paste with the same w/c (CK1, Figure 14b,d). As discussed, the porous nature of RC reduced the effective inter-particle spacing at a given w/c ratio, bringing particles closer together. Consequently, a more densely packed structure with refined porosity was achieved in RCK than in CK1.

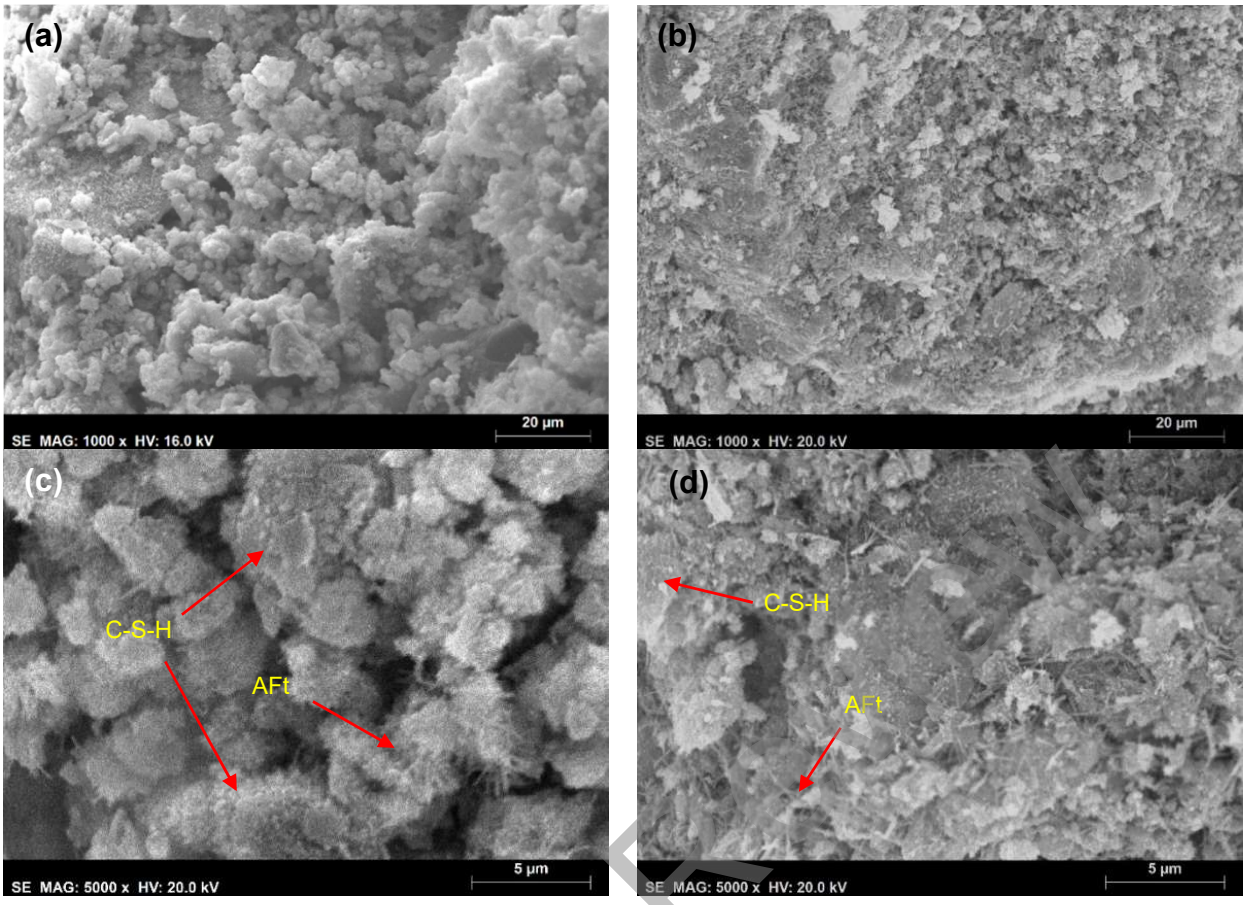

Figure 14 – SEM micrographs of CK1 (left) and RCK (right). RCK exhibited a denser pore structure with reduced inter-particle spacing compared to CK1: 12 h (a, b); 1 day (c, d).

Recycled cement exhibited a high rehydration capacity from early ages, forming the same types of hydration products as those observed in PC pastes. At 12 h, hydrated aluminate phases (AFt and AFm) predominated (Figure 14), as the α'_H−C_2S polymorph in RC was more effectively consumed after 1 day (section 3.2). In contrast to previous studies [45,46], abundant ettringite was detected from early ages (Figure 14,Figure 15). These hydrated products were mainly formed next to RC particles of high surface area. After 1 day, the accelerated hydration resulted in a more cohesive microstructure with apparently reduced pore connectivity compared to CK1 (Figure 14c,d). Over time, the hydration products progressively filled the inter-particle space, bridging particles and forming a continuous matrix composed of a complex mix of AFm, AFt, and C–S–H phases (Figure 15).

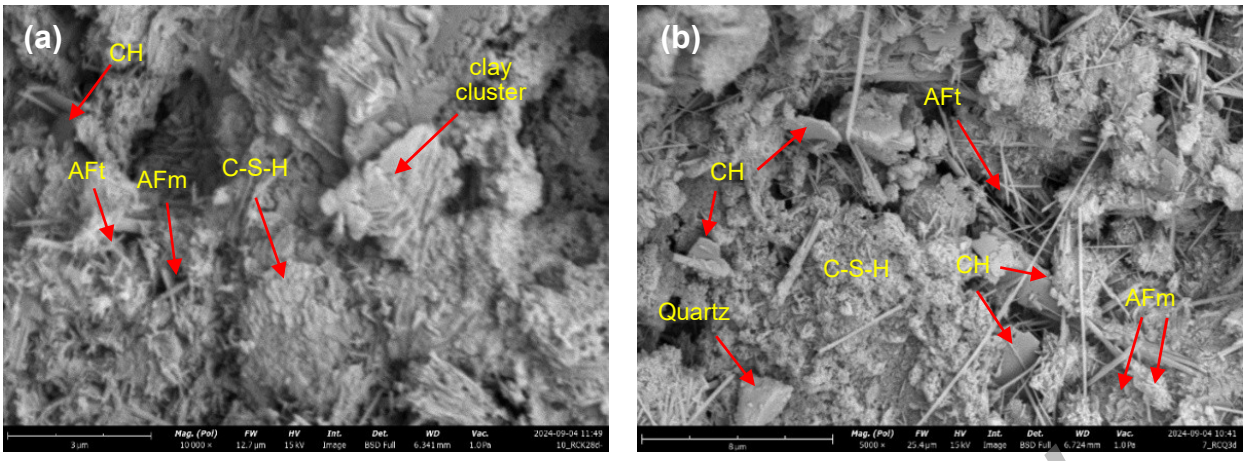

Figure 15 – SEM micrographs: (a) RCK at 28 days; (b) RCQ at 3 days.

Individual quartz or kaolinite particles were not easily distinguishable in SEM micrographs, as they were largely covered by or embedded within hydration products and well-integrated into the hydrated matrix, particularly at later ages. Most particles can only be identified by EDS, due to their high Si and Al contents, as well as the presence of K in illite/muscovite. In regions where clay particles were apparent, especially at early ages or within weaker zones, hydration products appeared to nucleate and grow at particle edges or other defective sites, as also reported by Liu et al. [10] (Figure 15 and Figure 16a–d). These sites of unsaturated chemical bonds can enable cation exchange and promote the deposition and growth of hydration products. Nucleation on clay particle surfaces was evident from the early stages of hydration (Figure 16a,g,h), with hydration products precipitating and growing near kaolinite and illite particles rather than within the inter-particle space (Figure 16g,h). While some clay sites were coated with bound hydration products, others appeared relatively clean or disconnected from them (Figure 16c–e). As expected, detected particles were less covered by hydration products, as they coincide with the fracture surface. Some instances show that hydration products were interposed between clay sheets, contributing to the cementation and stabilisation of flocculated clay particles (Figure 16e–g).

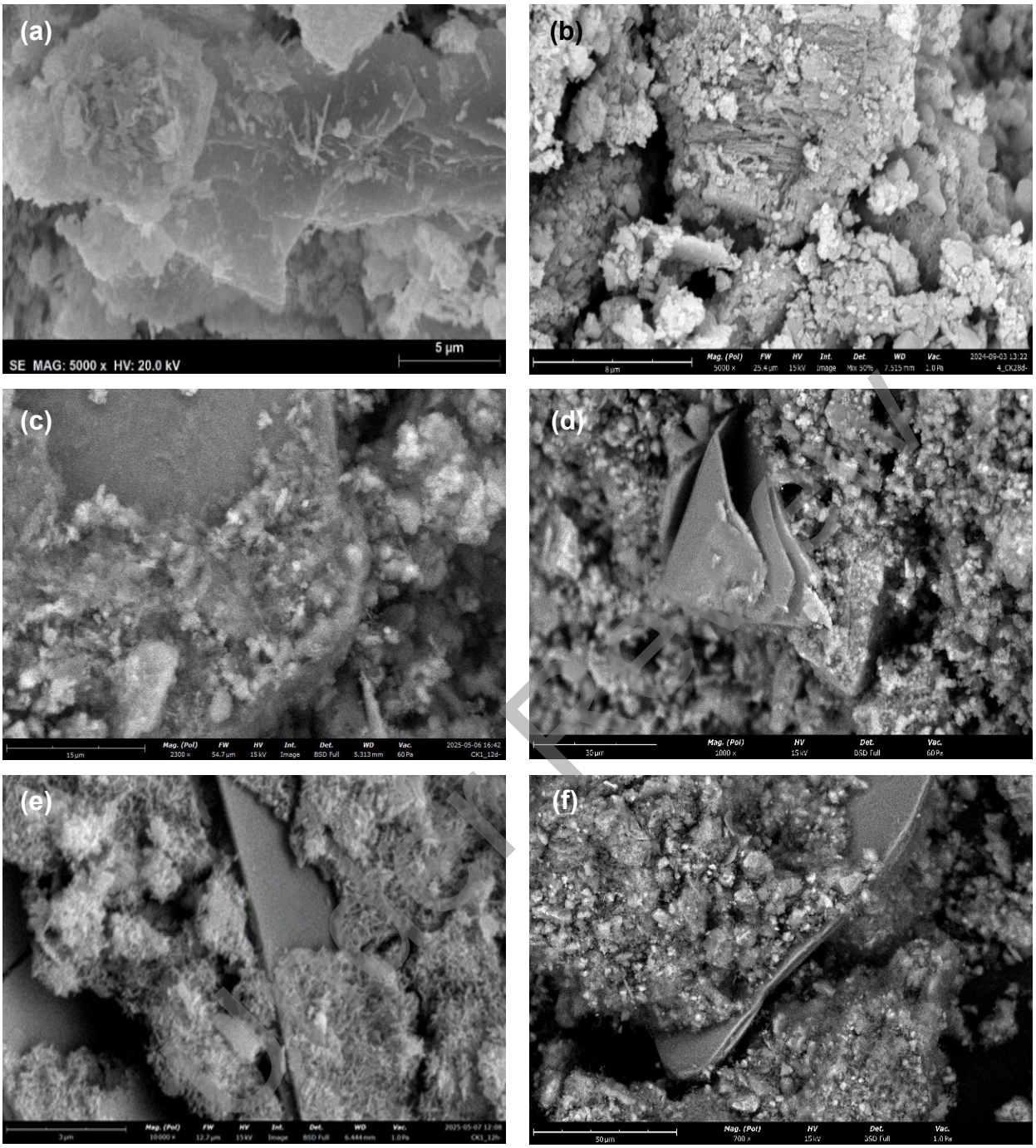

Figure 16 – SEM micrographs illustrating clay–cement interactions: (a) hydration products on the edges of clay surface (RCK at 12 h); (b) stacked clay aggregates coated with hydration products (CK at 28 days); (c) clay aggregate partially covered by hydration products (CK1 at 12 h); (d) illite sheets with hydration products precipitated on edges (CK1 at 12 h); (e) illite sheets intercalated and coated with hydration products, well interspersed within the cement matrix (CK1 at 12 h); (f) Illite particles embedded in the RC paste, with good interfacial affinity (RCK at 12 h).

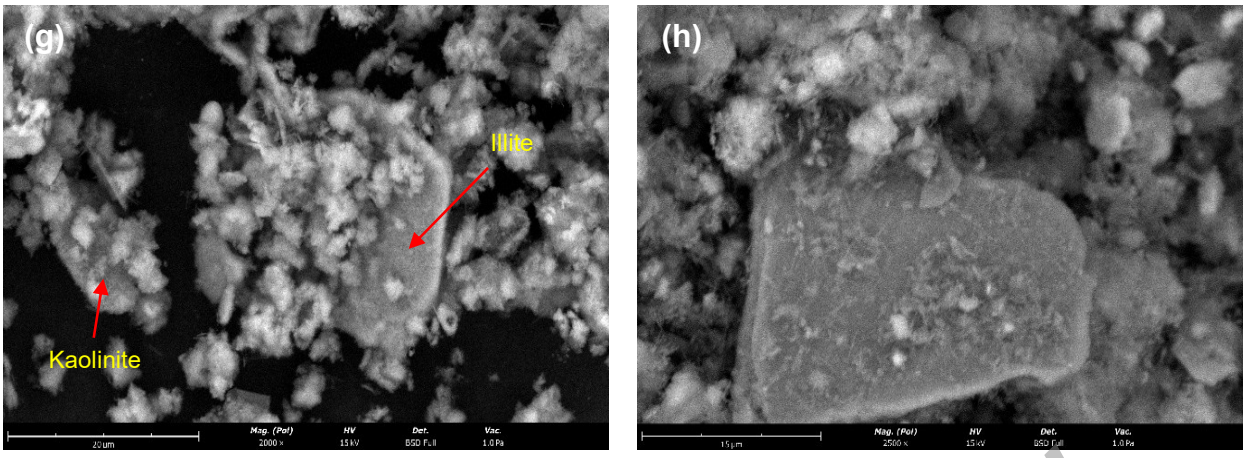

Figure 16 (cont.) – SEM micrographs illustrating clay–cement interactions: (g) hydration products nucleated and grown on the surfaces of kaolinite and illite particles (CK1 at 3 days); (h) heterogeneous nucleation of hydration products on clay surface (RCK at 12 h).

In accordance with sections 3.1–3.3, the formation of hydration products resulting from possible chemical reactions between kaolinite and cement was not significant. The slight reduction in CH content observed in mixtures containing kaolinite compared to the reference pastes without clay (section 3.1) was likely associated with the formation of limited surface products (C–S–H, C–A–S–H), as also reported by Mengliang et al. [24] for bentonite-containing pastes. This effect was more pronounced in PC pastes, which may be attributed to a better dispersion of clay particles in this system. Indeed, as illustrated in Figure 17, PC pastes exhibited a more homogeneous and less agglomerated microstructure than their RC counterparts.

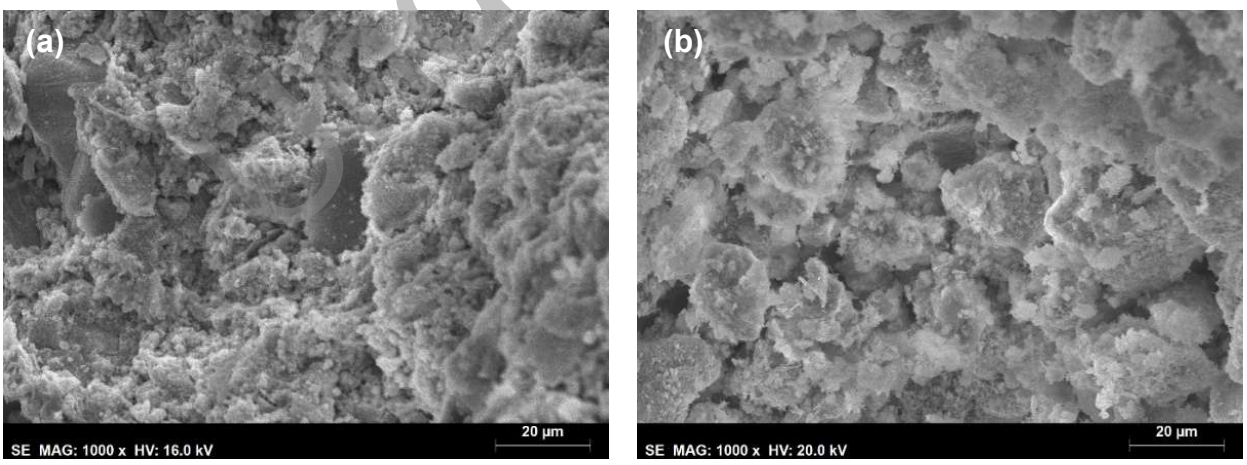

Figure 17 – SEM micrographs at 12 hours: (a) CK; (b) and RCK.

It is suggested that the high-water demand and irregular morphology of RC particles hinder the effective dispersion of kaolinite, thereby reducing its available surface area and

nucleation ability. This may explain the slightly reduced effectiveness of kaolinite in accelerating hydration in RC pastes compared with PC pastes (sections 3.1−3.3).

In summary, the hydration products exhibited good affinity for both quartz and kaolinite surfaces, progressively embedding the particles and filling the inter-particle spaces, regardless of the binder type. The high hydration capacity and appropriate bonding properties of RC are thereby confirmed, enabling the development of a dense and cohesive microstructure that is not adversely affected by clay–cement interactions.

3.7 Mechanical strength

As mentioned, due to its high water demand, RC pastes were prepared with higher w/c than PC pastes, resulting in lower fresh density and reduced mechanical strength (Table 7). Partial replacement of either PC or RC with quartz or clay led to an increase in fresh density and a reduction in workability, owing to the decrease in the w/b at constant w/c. The loss of workability was more pronounced in pastes containing clay than in those with quartz, reflecting the higher SSA and interparticle porosity of the clay. Consequently, clay-containing pastes showed slightly lower compactness, with a higher volume of voids, particularly when combined with RC (Table 7).

For these reasons, in pastes with equal w/c (CK1 vs. RCK), the use of RC led to a marked reduction in workability and an increase in the volume of voids. Nevertheless, the compressive strength of RCK was consistently higher than that of CK1 at all testing ages (Figure 18). This outcome corroborates the slightly higher hydration capacity and the more refined microstructure developed in RCK compared with CK1, as discussed in sections 3.1–3.4. The strength difference was more pronounced at early ages, which can be attributed to the fast reactivity of RC and the formation of a densely packed microstructure with reduced inter-particle spacing (sections 3.1 and 3.4). Similar trends have been reported in previous studies [45,94,113]. In contrast to the findings of Bogas et al. [46], the long-term compressive strength of RC pastes remained higher than that of PC pastes with the same w/c. On the one hand, the hydration rate of PC pastes tends to decrease at high w/c (section 3.1). On the other hand, although Zhang et al. [77] suggested that compressive strength may be limited by the porous nature and lower bearing strength of RC particles, this effect became less relevant in pastes with high w/c, where strength is mainly governed by inter-particle porosity. In addition, RC pastes exhibited a pronounced strength gain

between 1 and 3 days, in agreement with the trends observed in the TG (section 3.1) and XRD (section 3.2) analyses.

Table 7 – Fresh and hardened properties of cement pastes.

Mix	w/c	ρ_f (kg/m³)	V_v (%)	Spread (mm)	Flexural strength, f_{ctm} (MPa)						Compressive strength, f_{cm} (MPa)					
					12 h	1 d	3 d	7 d	28 d	90 d	12 h	1 d	3 d	7 d	28 d	90 d
C	0.5	1779	0.78	191	0.87	1.71	2.78	6.74	6.77	7.10	2.4	6.5	13.3	29.6	36.3	40.3
RCP	1.0	1458	2.84	204	0.21	0.82	1.48	1.78	2.24	2.66	0.5	2.9	6.8	7.8	10.9	12.5
CQ	0.5	1887	0.42	180	1.23	3.91	5.30	6.31	7.23	8.63	4.8	15.9	27.1	36.7	50.8	52.7
RCQ	1.0	1554	2.37	185	0.28	0.95	1.76	1.93	2.28	2.52	0.9	4.1	7.7	9.7	12.9	14.5
CK	0.5	1888	0.68	175	1.69	3.22	4.53	4.74	6.20	7.11	7.0	18.4	26.4	34.6	46.6	49.6
RCK	1.0	1529	4.20	155	0.37	0.88	1.74	2.18	2.51	2.77	1.1	3.9	8.5	9.4	12.7	13.3
CK1	1.0	1579	1.29	234	NP	0.70	1.52	NP	3.38	NP	NP	1.8	4.2	NP	9.1	NP

w/c – water to cement ratio; ρ_f – fresh density; V_v – volume of voids; NP – not performed

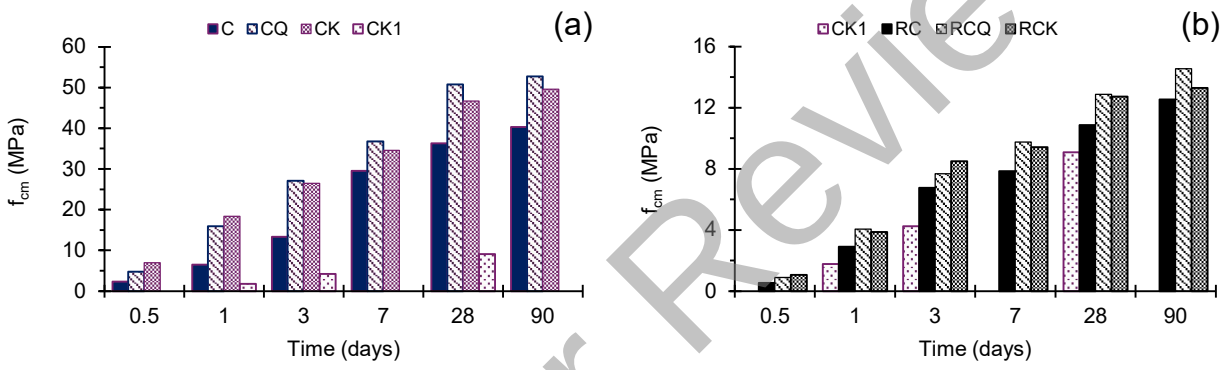

Figure 18 – Compressive strength of cement pastes from 12 hours to 90 days: (a) w/c = 0.52; (b) and w/c = 1.0.

Both quartz and clay additions enhanced the mechanical strength, resulting in 28-day compressive strengths that were 28–39% and 17–18% higher than those of the reference PC and RC pastes, respectively (Figure 18). Strength gain was even greater at early ages, reaching 2.4–2.8 and 1.3–1.4 times higher at 1 day, respectively. This effect is primarily attributed to the filler and nucleation provided by these fine additions. The higher early-age strength of pastes containing clay, particularly in PC systems, aligns with the hydration acceleration observed in section 3.1, driven by the high SSA and nucleation capacity of clay particles.

At 28 days, however, the compressive strength of pastes with clay was 2% (RC) and 8% (PC) lower than that of pastes with quartz (Table 7). This reduction was not due to adverse clay–cement interactions, since hydration was not hindered by the presence of clay (section 3.1) and the cement–clay interface bond was not weaker than that with quartz (section 3.6).

Instead, the slight strength decrease can be attributed to the lower intrinsic bearing capacity of clay particles, which has greater impact in PC pastes with low w/c and higher strength.

In general, the flexural strength follows the same trend of compressive strength (Figure 19). However, for a given compressive strength, pastes containing clay tended to display slightly lower tensile strength. This behaviour can be attributed to the greater sensitivity of tensile strength to the presence of weaker inclusions compared with compressive strength [114].

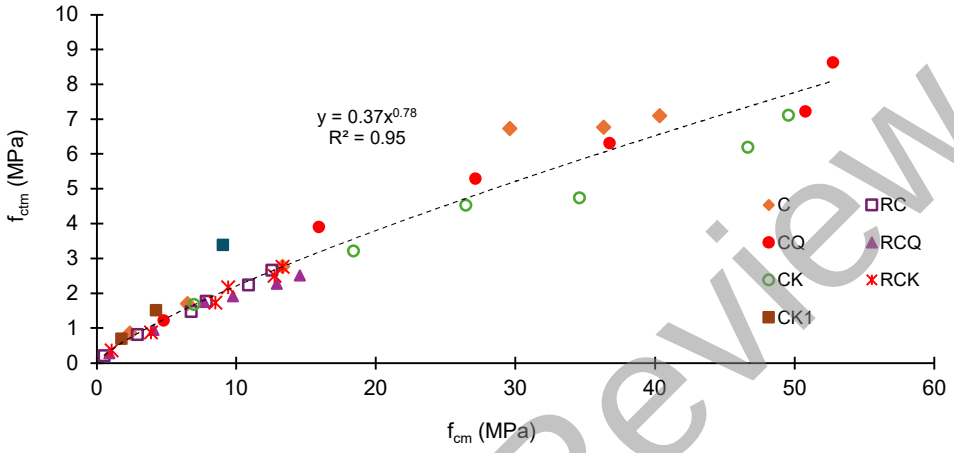

Figure 19 – Relationship between compressive (f_{cm}) and tensile (f_{ctm}) strength, from 12 hours to 90 days.

4. Conclusions

Clay–cement interactions were comprehensively analyzed in pastes with recycled cement (RC) and a kaolinite-rich clay, as well as in Portland cement (PC) pastes for comparison. Phase development and microstructural evolution were assessed using XRD, TG, NMR, SEM, MIP, and N_2A. The following key conclusions can be drawn:

- Recycled cement showed a high rehydration capacity, with a slightly higher hydration rate and faster formation of AFm phases than PC pastes at the same w/c. The predominant phase in RC pastes was α'_H–C_2S, which underwent substantial hydration during the first three days.
- Incorporating up to 25 vol % non-expanding clay minerals did not adversely affect cement hydration. Instead, nucleation effects promoted early hydration compared with reference non-blended pastes.
- Up to 28 days, no significant pozzolanic reactions occurred between PC or RC and kaolinite, as confirmed by TG, XRD, and NMR analyses. Minor clay–cement interactions

were observed in PC pastes with lower w/c, likely due to better clay dispersion, confirmed by NMR, which indicated slightly enhanced formation of C−(A−)S−H in these pastes.

- At the same w/c, RC pastes formed a more refined microstructure within the first three days than PC pastes, reflecting both the rapid rehydration of RC and the development of a dual microstructural network.
- Blended cements exhibited denser microstructures than plain pastes, regardless of the type of addition. Replacing PC with either clay or quartz led to comparable pore refinement, suggesting that clay influenced the microstructure mainly through physical mechanisms. Moreover, kaolinitic clay had negligible influence on long-term microstructural evolution, with minimal clay–cement interactions, as confirmed by MIP, N_2A, and SEM analyses.
- SEM analysis showed that clay particles provided sites for hydration products to nucleate and grow, exhibiting good affinity with both PC and RC. Moreover, hydration products effectively cemented clay particles by interposing between them, with better clay dispersion observed in PC pastes than in RC pastes.
- Due to its higher water demand and w/c, RC pastes had lower mechanical strength than PC pastes of similar workability. However, they developed higher mechanical strength than PC pastes with the same w/c, particularly at early ages. Clay particles enhanced early-age strength, but slightly reduced long-term strength due to their low load-bearing capacity, rather than any adverse cement-clay interaction.

In conclusion, recycled cement demonstrated good compatibility with non-expanding clay minerals, with no detrimental effects on hydration or microstructure development. Its performance was comparable to that of conventional cement, supporting its use as a more environmentally friendly alternative for earth stabilisation.

Acknowledgments

The authors acknowledge the Portuguese Foundation for Science and Technology (FCT, https://ror.org/00snfqn58) for funding this research through project PTDC/ECI-CON/0704/2021, and through the project UIDB/06438/2025 (https://doi.org/10.54499/UID/06438/2025) of the research unit CERIS. The first author also gratefully acknowledges the support of FCT through the doctoral scholarship referenced as 2023.05651.BD, with the DOI identifier https://doi.org/10.54499/2023.05651.BD.

References

[1] F. Bell, Cement Stabilization and Clay Soils, with Examples, Environmental & Engineering Geoscience 1 (1995) 139–151. https://doi.org/10.2113/gseegeosci.I.2.139.

[2] J. Prusinski, S. Bhattacharja, Effectiveness of Portland Cement and Lime in Stabilizing Clay Soils, Transp. Res. Rec. 1652 (1999) 215–227. https://doi.org/10.3141/1652-28.

[3] B. Medvey, G. Dobszay, Durability of Stabilized Earthen Constructions: A Review, Geotechnical and Geological Engineering 38 (2020) 2403–2425. https://doi.org/10.1007/s10706-020-01208-6.

[4] S. Horpibulsuk, N. Miura, T.S. Nagaraj, Assessment of strength development in cement-admixed high water content clays with Abrams' law as a basis, Géotechnique 53 (2003) 439–444. https://doi.org/10.1680/geot.2003.53.4.439.

[5] H. Miraki, N. Shariatmadari, P. Ghadir, S. Jahandari, Z. Tao, R. Siddique, Clayey soil stabilization using alkali-activated volcanic ash and slag, Journal of Rock Mechanics and Geotechnical Engineering 14 (2022) 576–591. https://doi.org/10.1016/J.JRMGE.2021.08.012.

[6] M.L. Nehdi, Clay in cement-based materials: Critical overview of state-of-the-art, Constr. Build. Mater. 51 (2014) 372–382. https://doi.org/10.1016/J.CONBUILDMAT.2013.10.059.

[7] H. Lindgreen, J. Skibsted, H. Krøyer, H. Jakobsen, Hydration of Portland Cement in the Presence of Clay Minerals Studied by 29Si and 27Al MAS NMR Spectroscopy, Advances in Cement Research 15 (2003) 103–112. https://doi.org/10.1680/adcr.2003.15.3.103.

[8] A. Herzog, J. Mitchell, Reactions Accompanying Stabilization of Clay with Cement, Highway Research Record (1963) 146–171.

[9] N. Rakhimova, Montmorillonite clays in Portland clinker-reduced, non-clinker cements, and cement composites: A review, Constr. Build. Mater. 411 (2024) 134678. https://doi.org/10.1016/J.CONBUILDMAT.2023.134678.

[10] L. Liu, Y. Li, Y. Wu, S. Luo, J. Peng, Y. Deng, G. Zhang, Strengthening mechanisms in cement-stabilized kaolinite revealed by cross-scale nanoindentation, Acta Geotech. 17 (2022) 5113–5132. https://doi.org/10.1007/s11440-022-01493-w.

[11] S. Horpibulsuk, Strength and Microstructure of Cement Stabilized Clay, in: V. Kazmiruk (Ed.), Scan. Electron Microsc., IntechOpen, London, 2012: pp. 439–460. https://doi.org/10.5772/35225.

[12] J. Wu, L. Liu, Y. Deng, G. Zhang, A. Zhou, Q. Wang, Distinguishing the effects of cementation versus density on the mechanical behavior of cement-based stabilized clays, Constr. Build. Mater. 271 (2021) 121571. https://doi.org/10.1016/J.CONBUILDMAT.2020.121571.

[13] C. Shi, R. Zhao, X. Wang, W. Wang, K. Ding, Effect of clay content on concrete properties, Case Studies in Construction Materials 20 (2024) e03341. https://doi.org/10.1016/J.CSCM.2024.E03341.

[14] J. Norvell, J. Steward, M. Juenger, D. Fowler, Influence of Clays and Clay-Sized Particles on Concrete Performance, Journal of Materials in Civil Engineering 19 (2007) 1053–1059. https://doi.org/10.1061/(ASCE)0899-1561(2007)19:12(1053).

[15] H. Choudhary, M.A. Siddiqui, D. Saha, Effect of Clay Fines on Strength and Workability of Concrete, Journal of Civil Engineering and Environmental Technology 6 (2019) 311–315. http://www.krishisanskriti.org/Publication.html.

[16] S.U. Rehman, U.A. Kiani, M. Yaqub, T. Ali, Controlling natural resources depletion through Montmorillonite replacement for cement-low cost construction, Constr. Build. Mater. 232 (2020) 117188. https://doi.org/10.1016/J.CONBUILDMAT.2019.117188.

[17] D. Noble, R. Plaster, Reactions in Portland Cement-Clay Mixtures (No. VHRC 70-R13), Virginia Transportation Research Council (VTRC), Charlottesville, Virginia, 1970.

[18] M.N. Haque, No-slump concrete with fine sand and clay, Cem. Concr. Res. 11 (1981) 531–539. https://doi.org/10.1016/0008-8846(81)90082-X.

[19] J. Wu, Z. Deng, Y. Deng, A. Zhou, Y. Zhang, Interaction between cement clinker constituents and clay minerals and their influence on the strength of cement-based

stabilized soft clay, Canadian Geotechnical Journal 59 (2021) 889–900. https://doi.org/10.1139/cgj-2021-0194.

[20] H. Lindgreen, M. Geiker, H. Krøyer, N. Springer, J. Skibsted, Microstructure engineering of Portland cement pastes and mortars through addition of ultrafine layer silicates, Cem. Concr. Compos. 30 (2008) 686–699. https://doi.org/10.1016/J.CEMCONCOMP.2008.05.003.

[21] J. Munoz, I. Tejedor, M. Anderson, S. Cramer, Effects of Coarse Aggregate Clay-Coatings on Concrete performance, Journal of Materials in Civil Engineering 22 (2005) 96–103. https://doi.org/https://doi.org/10.1061/(ASCE)0899-1561(2010)22:1(96).

[22] L. Keke, L. Yong, X. Liuliu, Z. Junjie, L. Kangning, F. Dingqiang, Y. Rui, Rheological characteristics of Ultra-High performance concrete (UHPC) incorporating bentonite, Constr. Build. Mater. 349 (2022) 128793. https://doi.org/10.1016/J.CONBUILDMAT.2022.128793.

[23] S.H. Chew, A.H.M. Kamruzzaman, F.H. Lee, Physicochemical and Engineering Behavior of Cement Treated Clays, Journal of Geotechnical and Geoenvironmental Engineering 130 (2004) 696–706. https://doi.org/10.1061/(ASCE)1090-0241(2004)130:7(696).

[24] M. Liu, Y. Hu, Z. Lai, T. Yan, X. He, J. Wu, Z. Lu, S. Lv, Influence of various bentonites on the mechanical properties and impermeability of cement mortars, Constr. Build. Mater. 241 (2020) 118015. https://doi.org/10.1016/J.CONBUILDMAT.2020.118015.

[25] K. Shafiei, Study of the Mortar and Concrete Properties with the Use of Raw Clay Minerals and Modified Calcareous Fly Ash, PhD Thesis, Technische Universität Berlin - TU Berlin, 2017.

[26] V.A. Fernandes, P. Purnell, G.T. Still, T.H. Thomas, The effect of clay content in sands used for cementitious materials in developing countries, Cem. Concr. Res. 37 (2007) 751–758. https://doi.org/10.1016/J.CEMCONRES.2006.10.016.

[27] N. Latifi, C.L. Meehan, M.Z.A. Majid, S. Horpibulsuk, Strengthening montmorillonitic and kaolinitic clays using a calcium-based non-traditional additive: A micro-level

study, Appl. Clay Sci. 132–133 (2016) 182–193. https://doi.org/10.1016/J.CLAY.2016.06.004.

[28] M. Chi, R. Huang, Effect of montmorillonite as additive on the properties of cement-based composites, Science and Engineering of Composite Materials 19 (2012) 45–54. https://doi.org/doi:10.1515/secm-2011-0129.

[29] H. Yang, D. Long, L. Zhenyu, H. Yuanjin, Y. Tao, H. Xin, W. Jie, L. Zhongyuan, L. Shuzhen, Effects of bentonite on pore structure and permeability of cement mortar, Constr. Build. Mater. 224 (2019) 276–283. https://doi.org/10.1016/J.CONBUILDMAT.2019.07.073.

[30] K.M. Ali, S.-N. Aref, B. Ali, S.-N. Adel, M. Ebrahim, Microstructural Characterization and Mechanical Properties of Cementitious Mortar Containing Montmorillonite Nanoparticles, Journal of Materials in Civil Engineering 28 (2016) 04016155. https://doi.org/10.1061/(ASCE)MT.1943-5533.0001671.

[31] C.R. Penson, Calcined calcium bentonite clay as a partial replacement of Portland cement in mortar, MsC Thesis, University of British Columbia, 2019. https://open.library.ubc.ca/collections/24/items/1.0376847.

[32] M.A. Mirgozar Langaroudi, Y. Mohammadi, Effect of nano-clay on workability, mechanical, and durability properties of self-consolidating concrete containing mineral admixtures, Constr. Build. Mater. 191 (2018) 619–634. https://doi.org/10.1016/J.CONBUILDMAT.2018.10.044.

[33] X. Gu, H. Tan, X. He, J. Zhang, X. Deng, Z. Zheng, M. Li, J. Yang, Improvement in flexural strength of Portland cement by lamellar structured montmorillonite, Constr. Build. Mater. 329 (2022) 127208. https://doi.org/10.1016/J.CONBUILDMAT.2022.127208.

[34] V. Sousa, J.A. Bogas, Comparison of energy consumption and carbon emissions from clinker and recycled cement production, J. Clean. Prod. 306 (2021) 127277. https://doi.org/10.1016/j.jclepro.2021.127277.

[35] O. Izemmouren, A. Guettala, S. Guettala, Mechanical Properties and Durability of Lime and Natural Pozzolana Stabilized Steam-Cured Compressed Earth Block

Bricks, Geotechnical and Geological Engineering 33 (2015) 1321–1333. https://doi.org/10.1007/s10706-015-9904-6.

[36] D. C. Sekhar, S. Nayak, Utilization of granulated blast furnace slag and cement in the manufacture of compressed stabilized earth blocks, Constr. Build. Mater. 166 (2018) 531–536. https://doi.org/10.1016/j.conbuildmat.2018.01.125.

[37] T.E. Elahi, A.R. Shahriar, M.S. Islam, Engineering characteristics of compressed earth blocks stabilized with cement and fly ash, Constr. Build. Mater. 277 (2021) 122367. https://doi.org/10.1016/j.conbuildmat.2021.122367.

[38] A. Carriço, J. Bogas, M. Guedes, Thermoactivated cementitious materials – A review, Constr. Build. Mater. 250 (2020). https://doi.org/10.1016/j.conbuildmat.2020.118873.

[39] A. Carriço, S. Real, J. Bogas, M. Pereira, Mortars with thermo activated recycled cement: Fresh and mechanical characterisation, Constr. Build. Mater. 256 (2020) 119502. https://doi.org/10.1016/j.conbuildmat.2020.119502.

[40] A. Carriço, J.A. Bogas, S. Real, M.F.C. Pereira, Shrinkage and sorptivity of mortars with thermoactivated recycled cement, Constr. Build. Mater. 333 (2022) 127392. https://doi.org/10.1016/J.CONBUILDMAT.2022.127392.

[41] S. Real, J.A. Bogas, A. Carriço, S. Hu, Mechanical characterisation and shrinkage of thermoactivated recycled cement concrete, Applied Sciences (Switzerland) 11 (2021) 2454. https://doi.org/10.3390/app11062454.

[42] A. Carriço, S. Real, J.A. Bogas, Durability performance of thermoactivated recycled cement concrete, Cem. Concr. Compos. 124 (2021) 104270. https://doi.org/10.1016/j.cemconcomp.2021.104270.

[43] J. Wang, M. Mu, Y. Liu, Recycled cement, Constr. Build. Mater. 190 (2018) 1124–1132. https://doi.org/10.1016/J.CONBUILDMAT.2018.09.181.

[44] R. Baldusco, T.R.S. Nobre, S.C. Angulo, V.A. Quarcioni, M.A. Cincotto, Dehydration and Rehydration of Blast Furnace Slag Cement, Journal of Materials in Civil Engineering 31 (2019) 04019132. https://doi.org/10.1061/(asce)mt.1943-5533.0002725.

[45] J.A. Bogas, A. Carriço, A.J. Tenza-Abril, Microstructure of thermoactivated recycled cement pastes, Cem. Concr. Res. 138 (2020) 106226. https://doi.org/10.1016/j.cemconres.2020.106226.

[46] J.A. Bogas, S. Real, A. Carriço, J.C.C. Abrantes, M. Guedes, Hydration and phase development of recycled cement, Cem. Concr. Compos. 127 (2022) 104405. https://doi.org/10.1016/j.cemconcomp.2022.104405.

[47] A. Carriço, J.A. Bogas, S. Hu, S. Real, M.F.C. Pereira, Novel separation process for obtaining recycled cement and high-quality recycled sand from waste hardened concrete, J. Clean. Prod. 309 (2021). https://doi.org/10.1016/j.jclepro.2021.127375.

[48] V. Sousa, J.A. Bogas, S. Real, I. Meireles, A. Carriço, Recycled cement production energy consumption optimization, Sustain. Chem. Pharm. 32 (2023). https://doi.org/10.1016/j.scp.2023.101010.

[49] V. Sousa, J.A. Bogas, S. Real, I. Meireles, Industrial production of recycled cement: energy consumption and carbon dioxide emission estimation, Environmental Science and Pollution Research 30 (2023) 8778–8789. https://doi.org/10.1007/s11356-022-20887-7.

[50] S. Real, V. Sousa, I. Meireles, J.A. Bogas, A. Carriço, Life Cycle Assessment of Thermoactivated Recycled Cement Production, Materials 15 (2022). https://doi.org/10.3390/ma15196766.

[51] R. Cruz, J.A. Bogas, Durability of compressed earth blocks stabilised with recycled cement from concrete waste and incorporating construction and demolition waste, Constr. Build. Mater. 450 (2024) 138673. https://doi.org/10.1016/j.conbuildmat.2024.138673.

[52] R. Cruz, J.A. Bogas, A. Balboa, P. Faria, Water resistance of compressed earth blocks stabilised with thermoactivated recycled cement, Materials 17 (2024). https://doi.org/10.3390/ma17225617.

[53] J.A. Bogas, S. Real, R. Cruz, B. Azevedo, Mechanical performance and shrinkage of compressed earth blocks stabilised with thermoactivated recycled cement, Journal of Building Engineering 79 (2023). https://doi.org/10.1016/j.jobe.2023.107892.

[54] S. Real, J.A. Bogas, R. Cruz, M.G. Gomes, M. Nabais, Thermal performance of compressed earth blocks stabilised with thermoactivated recycled cement, Energy Build. 314 (2024). https://doi.org/10.1016/j.enbuild.2024.114288.

[55] S. Real, J.A. Bogas, R. Cruz, M.G. Gomes, Eco-recycled cement's effect on the microstructure and hygroscopic behaviour of compressed stabilised earth blocks, Journal of Building Engineering 95 (2024). https://doi.org/https://doi.org/10.1016/j.jobe.2024.110227.

[56] L.N. Reddi, A.K. Jain, H.B. Yun, Soil materials for earth construction: Properties, classification and suitability testing, in: M. Hall, R. Lindsay, M. Krayenhoff (Eds.), Modern Earth Buildings: Materials, Engineering, Constructions and Applications, 1st ed., Woodhead Publishing Limited, 2012: pp. 155–171. https://doi.org/10.1533/9780857096166.2.155.

[57] W. Tabet, A. Cerato, A. Elwood Madden, R. Jentoft, Characterization of Hydration Products' Formation and Strength Development in Cement-Stabilized Kaolinite Using TG and XRD, Journal of Materials in Civil Engineering 30 (2018) 04018261. https://doi.org/10.1061/(ASCE)MT.1943-5533.0002454.

[58] EN 451-1, Method of testing fly ash - Part 1: Determination of free calcium oxide content, European Committee for Standardization (CEN), 2017.

[59] EN 196-2, Method of testing cement - Part 2: Chemical analysis of cement, European Committee for Standardization (CEN), 2013.

[60] EN 196-3, Methods of testing cement - Part 3: Determination of setting times and soundness, European Committee for Standardization (CEN), 2016.

[61] EN 196-5, Methods of testing cement - Part 5: Pozzolanicity test for pozzolanic cement, European Committee for Standardization, 2011.

[62] EN 1015-3, Methods of test for mortar for masonry - Part 3: Determination of consistence of fresh mortar (by flow table), European Committee for Standardization, 1999.

[63] K. Scrivener, A. Bazzoni, B. Mota, J. Rossen, Electron microscopy, in: K. Scrivener, R. Snellings, B. Lothenbach (Eds.), A Practical Guide to Microstructural Analysis of

Cementitious Materials, 1st ed., CRC Press, Boca Raton, 2016: pp. 353–417. https://doi.org/10.1201/b19074-9.

[64] F. Winnefeld, A. Scholer, B. Lothenbach, Sample preparation, in: K. Scrivener, R. Snellings, B. Lothenbach (Eds.), A Practical Guide to Microstructural Analysis of Cementitious Materials, 1st ed., CRC Press, Boca Raton, 2016: pp. 2–35. https://doi.org/10.1201/b19074-9.

[65] EN 1015-11, Methods of test for mortar for masonry - Part 11: Determination of flexural and compressive strength of hardened mortar, European Committee for Standardization (CEN), 2019.

[66] EN 1015-6, Methods of test for mortar for masonry - Part 6: Determination of bulk density of fresh mortar, European Committee for Standardization, 1998.

[67] W. Deboucha, N. Leklou, A. Khelidj, M.N. Oudjit, Hydration development of mineral additives blended cement using thermogravimetric analysis (TGA): Methodology of calculating the degree of hydration, Constr. Build. Mater. 146 (2017) 687–701. https://doi.org/10.1016/J.CONBUILDMAT.2017.04.132.

[68] B. Lothenbach, P. Durdzinski, K. De Weerdt, Thermogravimetric analysis, in: K. Scrivener, R. Snellings, B. Lothenbach (Eds.), A Practical Guide to Microstructural Analysis of Cementitious Materials, 1st ed., CRC Press, Boca Raton, 2016: pp. 177–211.

[69] R. Snellings, X-ray powder diffraction applied to cement, in: K. Scrivener, R. Snellings, B. Lothenbach (Eds.), A Practical Guide to Microstructural Analysis of Cementitious Materials, 1st ed., CRC Press, Boca Raton, 2016: pp. 107–176.

[70] K.L. Scrivener, T. Füllmann, E. Gallucci, G. Walenta, E. Bermejo, Quantitative study of Portland cement hydration by X-ray diffraction/Rietveld analysis and independent methods, Cem. Concr. Res. 34 (2004) 1541–1547. https://doi.org/10.1016/J.CEMCONRES.2004.04.014.

[71] S. Lowell, J. Shields, M. Thomas, M. Thommes, Characterization of Porous Solids and Powders: Surface Area, Pore Size and Density, 1st ed., Springer Dordrecht, Dordrecht, 2005.

[72] U. Kuila, Measurement and Interpretation of Porosity and Pore-Size Distribution in Mudrocks: The Hole Story of Shales, PhD thesis in Petroleum Engineering, Colorado School of Mines, 2013.

[73] R. Serpell, F. Zunino, Recycling of hydrated cement pastes by synthesis of α′H-C2S, Cem. Concr. Res. 100 (2017) 398–412. https://doi.org/10.1016/J.CEMCONRES.2017.08.001.

[74] H.N. Atahan, O.N. Oktar, M.A. Taşdemir, Effects of water–cement ratio and curing time on the critical pore width of hardened cement paste, Constr. Build. Mater. 23 (2009) 1196–1200. https://doi.org/10.1016/J.CONBUILDMAT.2008.08.011.

[75] D.P. Bentz, Influence of water-to-cement ratio on hydration kinetics: Simple models based on spatial considerations, Cem. Concr. Res. 36 (2006) 238–244. https://doi.org/10.1016/J.CEMCONRES.2005.04.014.

[76] Q. Zeng, K. Li, T. Fen-Chong, P. Dangla, Determination of cement hydration and pozzolanic reaction extents for fly-ash cement pastes, Constr. Build. Mater. 27 (2012) 560–569. https://doi.org/10.1016/J.CONBUILDMAT.2011.07.007.

[77] L. Zhang, Y. Ji, G. Huang, J. Li, Y. Hu, Modification and enhancement of mechanical properties of dehydrated cement paste using ground granulated blast-furnace slag, Constr. Build. Mater. 164 (2018) 525–534. https://doi.org/10.1016/j.conbuildmat.2017.12.232.

[78] K.B. Park, S.J. Kwon, X.Y. Wang, Analysis of the effects of rice husk ash on the hydration of cementitious materials, Constr. Build. Mater. 105 (2016) 196–205. https://doi.org/10.1016/J.CONBUILDMAT.2015.12.086.

[79] R. Hay, K. Celik, Effects of water-to-binder ratios (w/b) and superplasticizer on physicochemical, microstructural, and mechanical evolution of limestone calcined clay cement (LC3), Constr. Build. Mater. 391 (2023) 131529. https://doi.org/10.1016/J.CONBUILDMAT.2023.131529.

[80] Z. Feng, J. Zhao, G. Huang, W.V. Liu, Influence of water-to-binder ratios on the performance of limestone calcined clay cement-based paste for mining applications, Green and Smart Mining Engineering 1 (2024) 262–272. https://doi.org/10.1016/J.GSME.2024.08.001.

[81] P. Amirpasha, H. Daniel, S. Parviz, B.A. M, Monitoring of Sulfate Attack in Concrete by Al27 and Si29 MAS NMR Spectroscopy, Journal of Materials in Civil Engineering 27 (2015) 04014226. https://doi.org/10.1061/(ASCE)MT.1943-5533.0001175.

[82] A. Korpa, S. Dervishi, J. Volavsek, S. Gjyli, A. Andoni, 29Si and 27Al MAS NMR assessment of the C-(A-) S–H nanomolecular structure of Ultra-High-Performance Concrete (UHPC) modified with pyrogenic oxides, Journal of the Indian Chemical Society 99 (2022) 100443. https://doi.org/10.1016/J.JICS.2022.100443.

[83] J. Hjorth, J. Skibsted, H.J. Jakobsen, 29Si MAS NMR studies of portland cement components and effects of microsilica on the hydration reaction, Cem. Concr. Res. 18 (1988) 789–798. https://doi.org/10.1016/0008-8846(88)90104-4.

[84] J.J. Kim, M.K. Rahman, M.M. Reda Taha, Examining microstructural composition of hardened cement paste cured under high temperature and pressure using nanoindentation and 29Si MAS NMR, Appl. Nanosci. 2 (2012) 445–456. https://doi.org/10.1007/s13204-012-0058-z.

[85] A.C.A. Muller, K.L. Scrivener, J. Skibsted, A.M. Gajewicz, P.J. McDonald, Influence of silica fume on the microstructure of cement pastes: New insights from 1H NMR relaxometry, Cem. Concr. Res. 74 (2015) 116–125. https://doi.org/10.1016/J.CEMCONRES.2015.04.005.

[86] P. Rejmak, J.S. Dolado, M.J. Stott, A. Ayuela, 29Si NMR in Cement: A Theoretical Study on Calcium Silicate Hydrates, The Journal of Physical Chemistry C 116 (2012) 9755–9761. https://doi.org/10.1021/jp302218j.

[87] F. Brunet, T. Charpentier, C.N. Chao, H. Peycelon, A. Nonat, Characterization by solid-state NMR and selective dissolution techniques of anhydrous and hydrated CEM V cement pastes, Cem. Concr. Res. 40 (2010) 208–219. https://doi.org/10.1016/J.CEMCONRES.2009.10.005.

[88] J. Skibsted, High resolution solid-state nuclear magnetic resonance spectroscopy of portland cement-based systems, in: K. Scrivener, R. Snellings, B. Lothenbach (Eds.), A Practical Guide to Microstructural Analysis of Cementitious Materials, 1st ed., CRC Press, Boca Raton, 2016: pp. 353–417.

[89] M. Mantovani, A. Escudero, A.I. Becerro, Application of 29Si and 27Al MAS NMR spectroscopy to the study of the reaction mechanism of kaolinite to illite/muscovite, Clays Clay Miner. 57 (2009) 302–310. https://doi.org/10.1346/CCMN.2009.0570303.

[90] M. Magi, E. Lippmaa, A. Samoson, G. Engelhardt, A.R. Grimmer, Solid-state high-resolution silicon-29 chemical shifts in silicates, J. Phys. Chem. 88 (1984) 1518–1522. https://doi.org/10.1021/j150652a015.

[91] B. Walkley, J.L. Provis, Solid-state nuclear magnetic resonance spectroscopy of cements, Mater. Today Adv. 1 (2019) 100007. https://doi.org/10.1016/J.MTADV.2019.100007.

[92] D.L. Carroll, T.F. Kemp, T.J. Bastow, M.E. Smith, Solid-state NMR characterisation of the thermal transformation of a Hungarian white illite, Solid State Nucl. Magn. Reson. 28 (2005) 31–43. https://doi.org/10.1016/J.SSNMR.2005.04.001.

[93] J. Skibsted, H.J. Jakobsen, C. Hall, Quantification of calcium silicate phases in Portland cements by 29Si MAS NMR spectroscopy, Journal of the Chemical Society, Faraday Transactions 91 (1995) 4423–4430. https://doi.org/10.1039/FT9959104423.

[94] S. Real, A. Carriço, J.A. Bogas, M. Guedes, Influence of the treatment temperature on the microstructure and hydration behavior of thermoactivated recycled cement, Materials 13 (2020). https://doi.org/10.3390/ma13183937.

[95] Y. Dong, C. Feng, Q. Zhao, X. Liang, Study on the Structure of C-S-H Gels of Slag–Cement Hardened Paste by 29Si, 27Al MAS NMR, Appl. Magn. Reson. 50 (2019) 1345–1357. https://doi.org/10.1007/s00723-019-01152-6.

[96] M.J. Herrero, A. Fernández-Jiménez, A. Palomo, Studies About the Hydration of Hybrid “Alkaline-Belite” Cement, Front. Mater. 6 (2019) 66. https://doi.org/10.3389/fmats.2019.00066.

[97] J.J. Kim, M.K. Rahman, A.A. Al-Majed, M.M. Al-Zahrani, M.M. Reda Taha, Nanosilica effects on composition and silicate polymerization in hardened cement paste cured under high temperature and pressure, Cem. Concr. Compos. 43 (2013) 78–85. https://doi.org/10.1016/J.CEMCONCOMP.2013.07.002.

[98] K.L. Scrivener, A. Nonat, Hydration of cementitious materials, present and future, Cem. Concr. Res. 41 (2011) 651–665. https://doi.org/10.1016/J.CEMCONRES.2011.03.026.

[99] M.D. Andersen, H.J. Jakobsen, J. Skibsted, Incorporation of Aluminum in the Calcium Silicate Hydrate (C−S−H) of Hydrated Portland Cements: A High-Field 27Al and 29Si MAS NMR Investigation, Inorg. Chem. 42 (2003) 2280–2287. https://doi.org/10.1021/ic020607b.

[100] A. Brykov, A. Vasil'ev, M. Mokeev, Hydration of portland cement in the presence of aluminum-containing setting accelerators, Russian Journal of Applied Chemistry 86 (2013) 793–801. https://doi.org/10.1134/S1070427213060013.

[101] A. Mazur, P. Tolstoy, K. Sotiriadis, 13C, 27Al and 29Si NMR Investigation of the Hydration Kinetics of Portland-Limestone Cement Pastes Containing CH3-COO−-R+ (R=H or Na) Additives, Materials 15 (2022) 2004. https://doi.org/10.3390/ma15062004.

[102] J. Skibsted, H.J. Jakobsen, C. Hall, Quantitative Aspects of 27Al MAS NMR of Calcium Aluminoferrites, Advanced Cement Based Materials 7 (1998) 57–59. https://doi.org/https://doi.org/10.1016/S1065-7355(97)00017-5.

[103] G. Paul, E. Boccaleri, L. Buzzi, F. Canonico, D. Gastaldi, Friedel's salt formation in sulfoaluminate cements: A combined XRD and 27Al MAS NMR study, Cem. Concr. Res. 67 (2015) 93–102. https://doi.org/https://doi.org/10.1016/j.cemconres.2014.08.004.

[104] H. Justnes, I. Meland, J.O. Bjoergum, J. Krane, T. Skjetne, Nuclear magnetic resonance (NMR) —a powerful tool in cement and concrete research, Advances in Cement Research 3 (1990) 105–110. https://doi.org/10.1680/adcr.1990.3.11.105.

[105] M. Palacios, H. Kazemi-Kamyab, S. Mantellato, P. Bowen, Laser diffraction and gas adsorption techniques, in: K. Scrivener, R. Snellings, B. Lothenbach (Eds.), A Practical Guide to Microstructural Analysis of Cementitious Materials, 1st ed., CRC Press, Boca Raton, 2016: pp. 445–483.

[106] W.C. Conner, J.F. Cevallos-Candau, E.L. Weist, J. Pajares, S. Mendioroz, A. Cortes, Characterization of pore structure: porosimetry and sorption, Langmuir 2 (1986) 151–154. https://doi.org/10.1021/la00068a006.

[107] K.S.W. Sing, Physisorption of nitrogen by porous materials, Journal of Porous Materials 2 (1995) 5–8. https://doi.org/10.1007/BF00486564.

[108] J. Thomas, H. Jennings, A. Allen, The Surface Area of Hardened Cement Paste as Measured by Various Techniques, Concrete Science and Engineering 1 (1999) 45–64.

[109] M. Raouf Sh, S. Suzy A, Adsorption of Organic Vapors in Relation to Pore Structure of Hardened Portland Cement Paste, in: Symposium of Structure of Portland Cement and Concrete, Highway Research Board Special Report 98, 1966. pp. 123–134.

[110] W. Wang, P. Liu, M. Zhang, J. Hu, F. Xing, The Pore Structure of Phosphoaluminate Cement, Open Journal of Composite Materials 2 (2012) 104–112. https://doi.org/10.4236/ojcm.2012.23012.

[111] H.M. Jennings, P.D. Tennis, Model for the Developing Microstructure in Portland Cement Pastes, Journal of the American Ceramic Society 77 (1994) 3161–3172. https://doi.org/https://doi.org/10.1111/j.1151-2916.1994.tb04565.x.

[112] Y. Suda, T. Saeki, T. Saito, Relation between Chemical Composition and Physical Properties of C-S-H Generated from Cementitious Materials, Journal of Advanced Concrete Technology 13 (2015) 275–290. https://doi.org/10.3151/jact.13.275.

[113] J. Bogas, A. Carriço, M. Pereira, Mechanical characterization of thermal activated low-carbon recycled cement mortars, J. Clean. Prod. 218 (2019) 377–389. https://doi.org/10.1016/j.jclepro.2019.01.325.

[114] J.A. Bogas, R. Nogueira, Tensile strength of structural expanded clay lightweight concrete subjected to different curing conditions, KSCE Journal of Civil Engineering 18 (2014) 1780–1791. https://doi.org/10.1007/S12205-014-0061-X.